Supplementary Information

Integrating Unwonted Photoluminescence and Anti-thermal Quenching in Ba₂MgTeO₆ Double Perovskites for High-Performance Optical Thermometers

Nithin Jayan Suraja, Amrithakrishnan Bindhu, Sibi Kaithakkal Solaman and

Subodh Ganesanpotti*

Table S1. Refined Crystallographic parameters of BMTO

Formula	: Ba$_2$MgTeO$_6$					
Crystal system	: Tetragonal					
Space group	: *I*4/*m*					
Cell Parameters	: $a = b = 5.823(5)$ Å, $c = 8.116(5)$ Å, $V = 275.2$ Å^3					
Reliability factors	: $Rwp = 6.22$ %, $Rp = 4.37$ %, $GOF = 1.72$					
Atoms	Site	x	y	z	Occupancy	Beq (Å^2)
Ba1	4d	0.000(0)	0.500(0)	0.250(0)	1	1.60(0)
Mg1	2a	0.000(0)	0.000(0)	0.500(0)	1	1.15(0)
Te1	2b	0.000(0)	0.000(0)	0.000(0)	1	1.25(6)
O1	4e	0.256(8)	0.256(4)	0.000(0)	1	1.49(3)
O2	8h	0.000(0)	0.000(0)	0.246(3)	1	0.30(7)

For the double perovskite A$_2$BB'O$_6$ structure, the coordination number of A-site cations varies from 8 to 12 according to the distortion in the crystal structure, while the B-site and B' cations are coordinated by six oxygen atoms, creating an alternating arrangement of corner-sharing BO$_6$ and B'O$_6$ octahedra. A d^0 transition metal with a higher oxidation state is substituted at the B' site within the double perovskite structure, and layered ordering of A-site cations, and rocksalt ordering of B/B' cations occur. The cuboctahedral cavities formed within this framework were filled by the A site substituted cations.[1] Here, BMTO crystallizes in a tetragonal structure with spacegroup *I*4/*m*.[2] Ba^{2+} ions (A-site) are coordinated with 12 oxygen

atoms, and the Mg^{2+} (B-site) and Te^{6+} (B'- site) ions are coordinated with six oxygen atoms, creating an alternating arrangement of corner-sharing MgO_6 and TeO_6 octahedra. Ordering of B and B' substituted cations is quite common in double perovskites of the type $A_2BB'O_6$ if the charge difference between them is ≥ 2 and the size difference is greater than 0.1 Å.[3] Here, a rocksalt ordering is observed since the charge difference and size difference between the Mg^{2+} and Te^{6+} ions were 4 and 0.16 Å.

Table S2. Raman band assignments of BMTO

Internal			External
v_1 (cm^{-1})	v_2 (cm^{-1})	v_5 (cm^{-1})	T or L (cm^{-1})
722 736	536	412	130

The low energy external modes in the 10 – 300 cm^{-1} region include both liberational (L) and translational (T) lattice modes which are very sensitive to the lowering of symmetry due to the tilting of octahedra, while those in the 300 – 500 cm^{-1} region correspond to the bending motion (v_5) of oxygen octahedra. The bands in the 500 – 650 cm^{-1} and 650 – 750 cm^{-1} are designated as internal vibration modes v_2 and v_1, which is due to the asymmetric and symmetric stretching vibration of oxygen octahedra.[2,4,5] By group theoretical predictions, it is reported that double perovskites crystallized in cubic structure has a total of four Raman active modes while that crystallized in tetragonal structure will have a total of nine Raman active modes.[4,5]
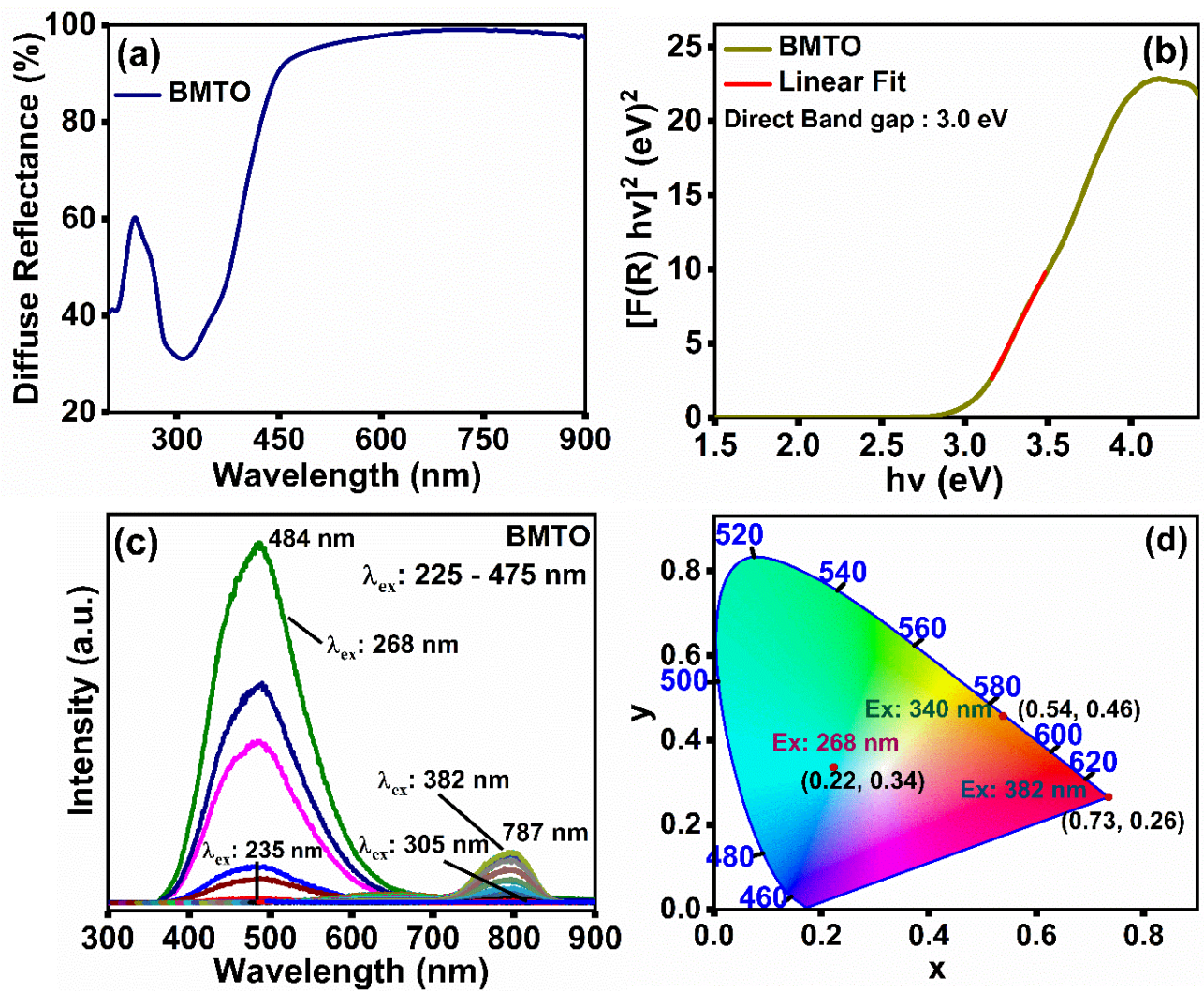
Fig. S1. (a) Diffuse reflectance spectra of BMTO, (b) Band gap of BMTO calculated using Kubelka-Munk function, (c) PL spectra of BMTO under various excitations. (d) CIE chromaticity diagram showing CIE coordinates under different excitations.

Table S3. Comparison of BMTO emission with the Te^{4+} emission

Material	Excitation (nm)	Emission Range (nm)	Emission Maxima (nm)	FWHM (nm)	Transition	Lifetime	Reference
BMTO	268	350-750	484	100	$^3T_{2u} \rightarrow ^1A_{1g}$ $^3T_{1u} \rightarrow ^1A_{1g}$	14.36 µs 66.03 µs	This work
Te^{4+} doped $YAl_3(BO_3)_4$	244	400-600	480	80	$^3T_{1u} \rightarrow ^1A_{1g}$	3.36 and 2.26 µs	[5]
Te^{4+} doped $YCa_4O(BO_3)_3$	310	340-450	384	50	$^3P_1, ^3P_0 \rightarrow ^1S_0$	2.28 & 22.66 µs)	[6]
Te^{4+} doped $CaYAlO_4$	325	650-800	715	40	$^3T_{1u}, ^3A_{1u} \rightarrow ^1A_{1g}$	0.34 & 1.54 ms	[7]
$Bi_{2-x}Te_xV_xO_3$	355	450-750	550	100	Oxygen vacancies	1.32 µs	[8]
$(C_2H_{20}N)_2TeCl_6$	437	460-720	600	130	STE		[9]
$Rb_2Sn_{1-x}TexCl_6$	405	480-720	630	150	$^3P_1 \rightarrow ^1S_0$	1925 ns to 596 ns (with increasing x)	[10]
Te^{4+} doped Cs_2ZrCl_6	250 390	350-750 450-750	400 460 575 575	115	Te^{4+} STE Zr^{4+} STE Te^{4+} triplet STE	2.91 &10.48(µs)	[11]

The luminescence decay behaviours of BMTO under 268 nm excitation and 484 nm emission wavelength and 382 nm excitation wavelength and 787 nm emission wavelength were studied (Fig. S2b-c) and the decay curve was well fitted by the bi-exponential function in Equation 1, and the average lifetime was calculated using Equation 2. [5,7]

$$I(t) = I_0 + A_1 \, exp \, (-t/\tau_1) + A_2 \, exp(-t/\tau_2) \tag{1}$$

$$\tau = (A_1 * \tau_1^2 + A_2 * \tau_2^2)/(A_1 * \tau_1 + A_2 * \tau_2) \tag{2}$$

where A_1 and A_2 are fitting constants while τ_1 and τ_2 are decay constants of lifetime with respect to each exponential component. The obtained average decay lifetime (τ) and R-square value were included in Fig. S2b-c.
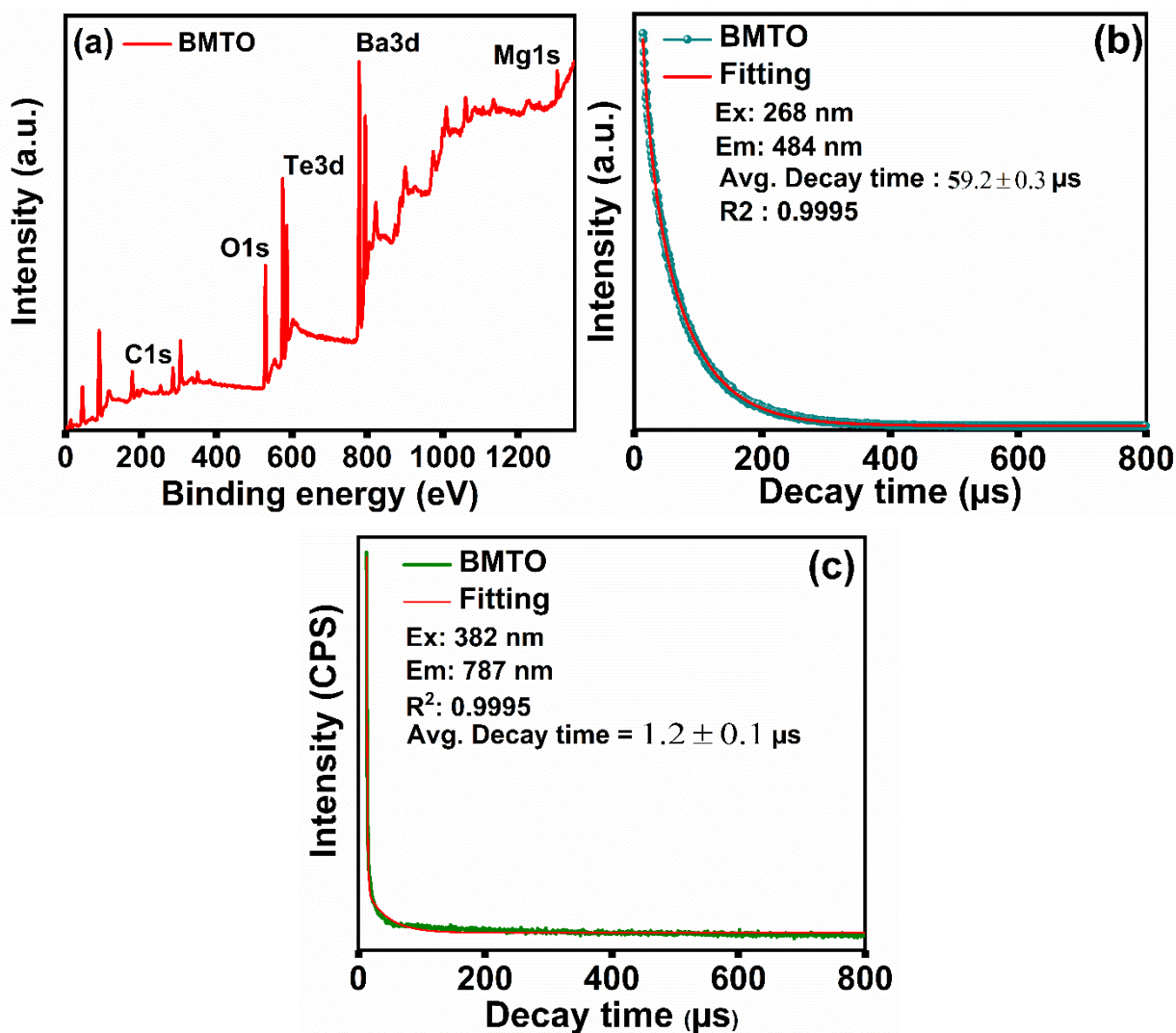
Fig. S 2. (a) XPS survey spectrum of BMTO, (b) The decay curve of BMTO under 268 nm excitation and 484 nm emission wavelength, (c) Decay curve of BMTO under 382 nm excitation and 787 nm emission wavelength.

The inherent luminescence of BMTO originates from the Te^{4+} ions within the host system. The term inherent luminescence indicates that the luminescence does not originate from any externally added impurities but it originates from the host itself. Recently the photoluminescence in Ba_2MgTeO_6 was patented by us which is the first report on the inherent luminescence within tellurate-based double perovskites without the aid of dopants.[12] followed by this an intrinsic near-infrared emission was observed and reported in $SrLaLiTeO_6$ under the excitation of UV radiation.[13] The use of intrinsic luminescence within BMTO for Vis-NIR emitting pc-LED applications was reported by us very recently.[14] The inherent luminescence in Ba_2MgTeO_6 is also observed by Cavalli et al. recently and the origin of emission is explained

5

in accordance with the Te^{4+} luminescence.[15] Very recently, a self-activated broadband NIR emission was reported in another double perovskite system Na_2ZrTeO_6, with the maximum emission at 780 nm.[16] Sariga et al. and Cavalli et al. reported that the intrinsic luminescence observed in tellurate double perovskites originates as a result of the electronic transitions among Te^{4+} ions and the presence of Te^{4+} is confirmed with the XPS analysis. Also, it is reported that the absence of complete oxidation of Te^{4+} to Te^{6+} ions causes the formation of Te^{4+} ions within the tellurate system. The Te^{4+} luminescence in these phosphors was attributed to the relaxation of electrons to the $^1A_{1g}$ ground state from the $^3T_{1u}$, and $^3A_{1u}$ excited states.[7,8] Hence with the above reports on the luminescence of tellurate-based systems, It is ensured that the luminescence in BMTO is mainly contributed by the Te^{4+} center.

Moreover, the possibility of defect luminescence in BMTO is also investigated. The possibility of emission from exterior impurities can be neglected since the phase purity of the material has already been confirmed by the Rietveld refinement of XRD patterns of BMTO and Raman analysis. Considering the large stokes shift observed, the chances of self-luminescent exciton recombination are almost improbable. The possibility of defect emission is also inspected by analyzing the temperature dependence of defect luminescence in previous reports. ZnO is a well-known material that is reported with defect luminescence. The literature suggests that defect luminescence in ZnO exhibits visible thermal dependence. With respect to the increase in temperature, the luminescent spectral profile of ZnO changes significantly. A shift in defect luminescence and the presence of additional bands with respect to temperature were also reported in such cases. Also, with respect to the annealing environment, the spectral profiles of ZnO defect emission show additional luminescence bands and exhibit a shift in emission peaks. With respect to temperature and annealing environment yellow, green and orange-red bands are observed in ZnO. Here it is suggested that yellow emission is attributed to the interstitial oxygen defects while the green emission corresponds to the oxygen deficiency. The orange-red emission is due to the presence of excess oxygen.[17] The temperature dependence of PL emission in BMTO was also analyzed. The emission profile of BMTO with temperature remains unchanged and is shown in Fig. 2 (c). Also, any additional bands or any shift in emission were not observed with respect to temperature. Only a decrease in luminescence intensity at higher temperatures was observed due to the thermal quenching effect. Since no changes such as the presence of an additional band and spectral shift with respect to temperature were not observed in our present system the hypothesis of luminescence due to defects can be discarded.

Further, an attempt was made to synthesize BMTO under various preparation conditions. BMTO was not formed while calcinating at 1150 ºC under nitrogen atmosphere. Because it is not possible to synthesize BMTO under a reducing atmosphere since the formation of a pure BMTO phase requires favourable thermodynamic conditions for the oxidation of Te^{4+} to Te^{6+}.

Next BMTO was annealed at the nitrogen atmosphere in order to check any change in PL emission. The Raman spectra of pure BMTO and BMTO annealed at different temperatures are shown in Fig. S3. It is found that the Raman profiles of annealed samples exhibit significant change in their spectral profiles which indicates that the annealed samples are not phase pure. This is because the proper oxidation of Te^{4+} to Te^{6+} did not take place under the N_2 atmosphere.
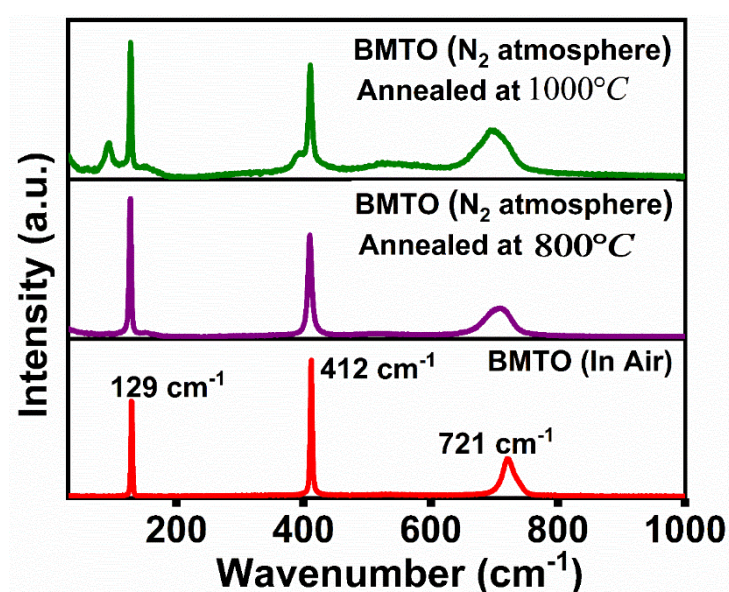

Fig. S3 Raman spectra of BMTO and annealed sample in nitrogen atmosphere at 800ºC and 1000ºC.

Further, the BMTO was synthesized under an oxygen atmosphere at 1150 ºC. The XRD patterns of as prepared sample were fitted with a tetragonal structure and the corresponding Lebail fit was shown in Fig. S4. The presence of impurities in the XRD patterns indicates that the sample is not phase pure.
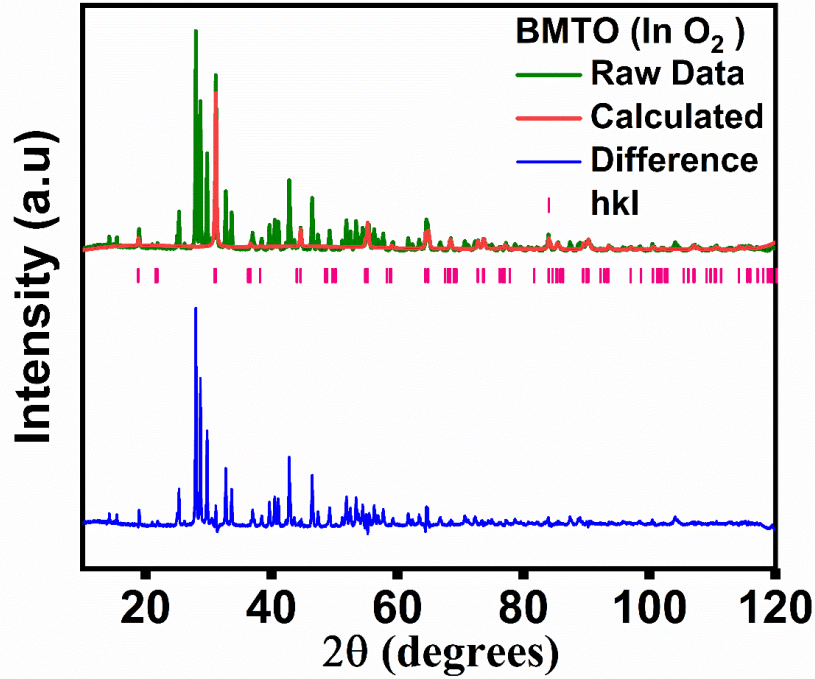
Fig. S4 Lebail fit of XRD patterns of BMTO synthesized under oxygen atmosphere.

Thereafter the phase pure sample was annealed in an oxygen atmosphere under 1000 ºC and 1100 ºC. The XRD patterns of BMTO annealed at oxygen atmosphere were well fitted with the tetragonal structure (*I4/m*) and the corresponding Lebail fit was shown in Fig. S5 (a)-(b). The absence of impurity peaks confirms the phase purity of the sample.
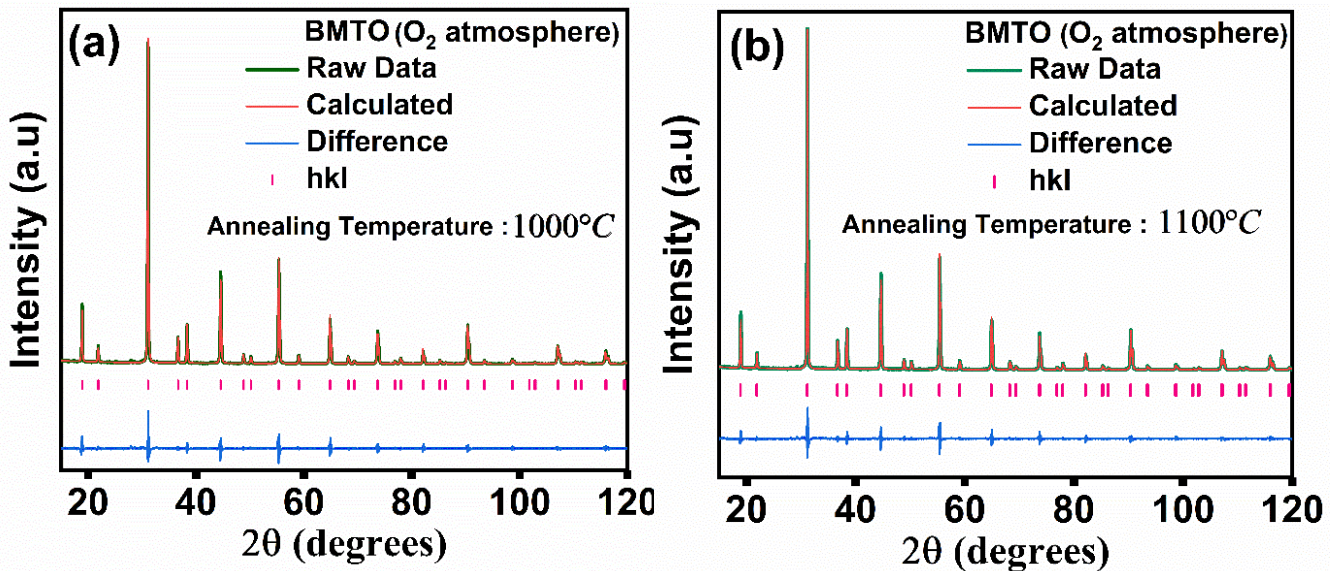

Fig. S5 Lebail fit of XRD patterns of BMTO annealed in oxygen atmosphere at (a) 1000ºC and (b) 1100ºC.

The Raman spectra of BMTO and O_2 annealed samples (Fig. S6) were also analyzed and the similar spectral profiles indicate similar structure for all the samples. The absence of additional bands in Raman spectra with respect to oxygen annealing ensures the absence of defect centres within BMTO.
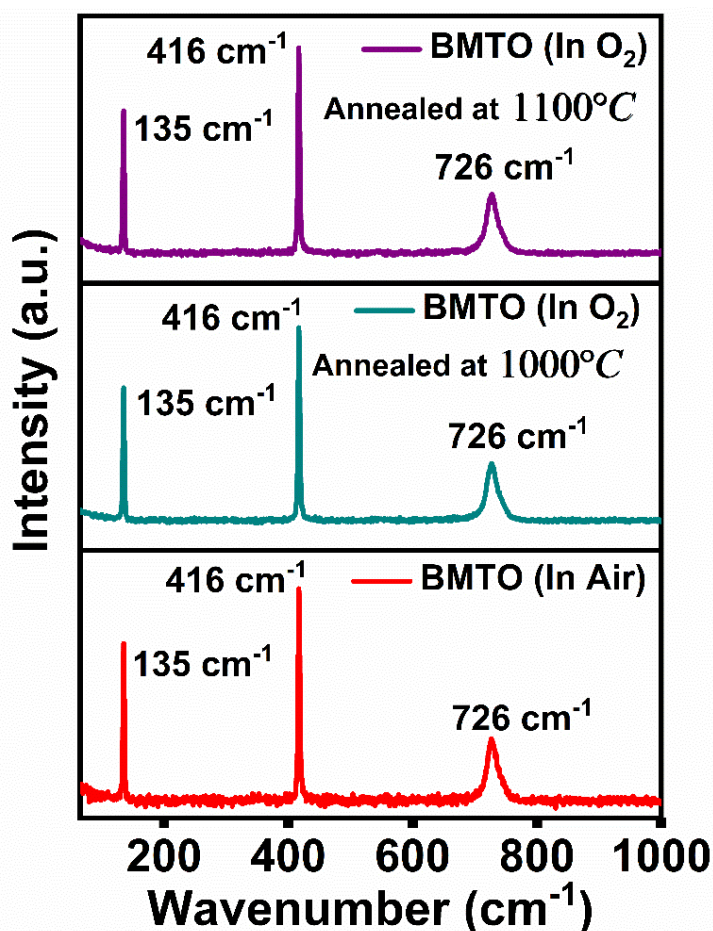

Fig. S6 Raman spectra BMTO, BMTO annealed at 1000ºC and 1100ºC.

Moreover, the diffuse reflectance spectra and the corresponding Kubelka Munk plots of BMTO and O_2 annealed samples were analyzed and are shown in Fig. S7 (a)-(c). Similar diffuse reflectance spectra and band gap energy were obtained for all the samples. The band gap energy of BMTO is 3.0 eV. Here it can be noted that the optical bandgap of the BMTO remains unchanged even after O_2 annealing at various temperatures- 1000^0C and 1100^0C. Thus, the optical bandgap in the BMTO is determined by the orbital components in the conduction band and energy levels in the Te^{4+} in the forbidden band and hence the emission from the BMTO system is mainly contributed by the Te^{4+} rather than O_2 vacancy-induced luminescence.
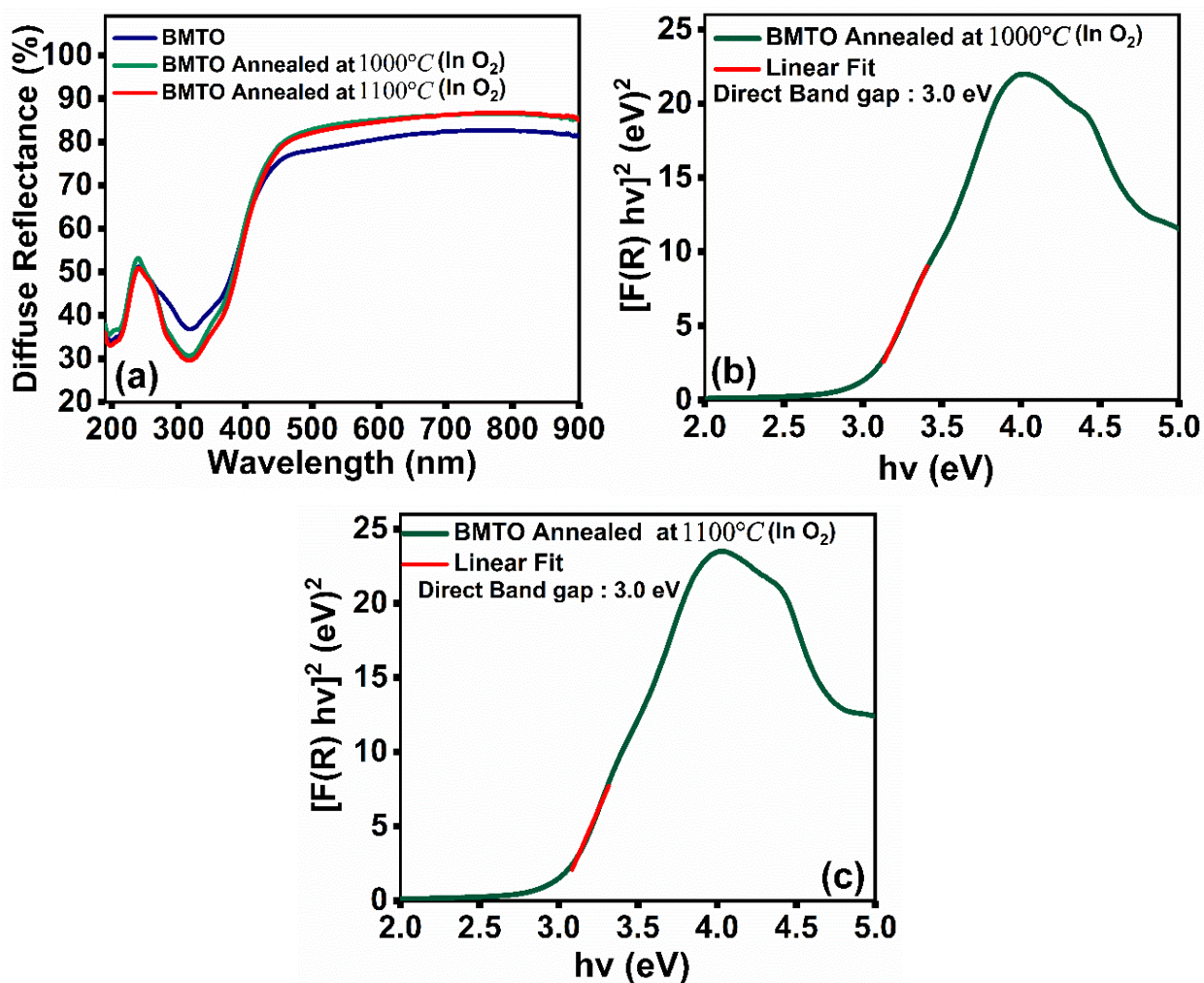
Fig. S7 (a) Diffuse reflectance spectra of BMTO and annealed samples in an oxygen atmosphere, Kubelka Munk plots of (b) BMTO annealed at 1000⁰C (c) BMTO annealed at 1100⁰C.

Further, the variation of PL emission with respect to oxygen annealing was analyzed and is shown in Fig. S8. Any change in the spectral profile or spectral shift was not observed with respect to oxygen annealing. Only a slight decrease in PL emission intensity was observed and this might be due to the decrease in Te^{4+} content while increasing in annealing temperature. While increasing the annealing temperature up to 1000 ⁰C a reduction in PL intensity by 25% is observed when compared to the PL intensity of pure BMTO. Also, there is no shift or additional bands were observed. This indicates that, even at higher annealing temperatures, only a few Te^{4+} ions oxidise to the Te^{6+} state, which causes a reduction in the intensity of emission, which further testifies that the origin of emission is contributed by Te^{4+} ions, not by O_2 vacancy induced luminescence.
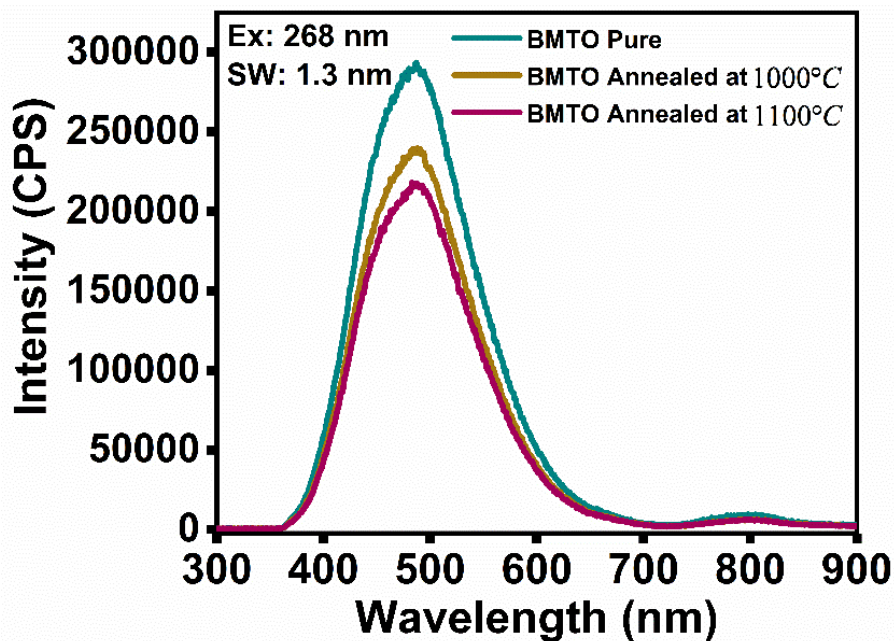
Fig. S8. PL emission spectra of BMTO and annealed samples

In addition, the decay lifetime was also calculated and is shown in Fig. S9. The decay curve was well-fitted by using a double exponential function. In the previous reports, the decay curve of Te^{4+} luminescence was fitted by a double exponential function and explains it with the dual transitions within Te^{4+} ions. A slight decrease in the decay time is noted with the O_2 annealing temperature, which agrees with the observed decrease in the PL intensity due to the decrease in Te^{4+} content. This again confirms that the luminescence originates from Te^{4+} ions but not from defect centres.
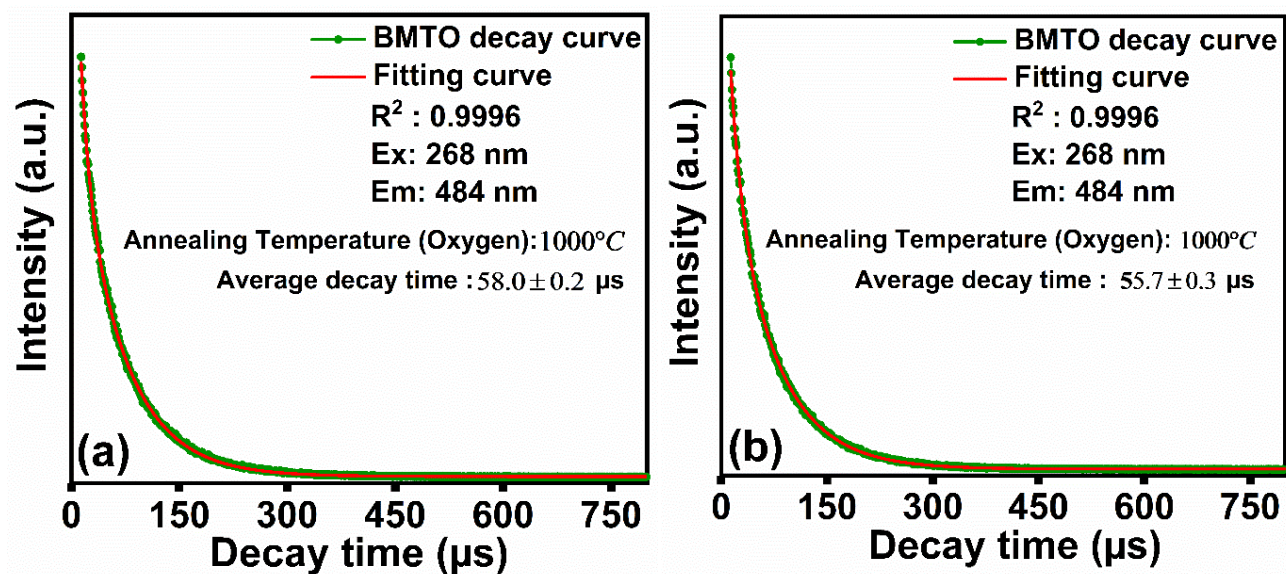

Fig. S9. The decay curves of BMTO annealed at (a) 1000ºC and (b) 1100ºC

In order to confirm the presence of Te^{4+} ions XPS analyses were carried out. The Te^{4+}/Te^{6+} ratio was estimated from the high-resolution XPS Te3d scan and is shown in Fig. S10. It is found that the Te^{4+}/Te^{6+} ratio decreases with respect to the increase in annealing temperature which is in agreement with the above-mentioned results obtained from DRS, PL, and decaytime. The similar XRD patterns, Raman profiles, DRS, bandgap energies, PL spectral profiles and decay lifetime ensure the absence of defect luminescence and confirm the origin of luminescence is due to Te^{4+} ions. Consequently, the chances of O_2 vacancy-induced luminescence in BMTO can be neglected.
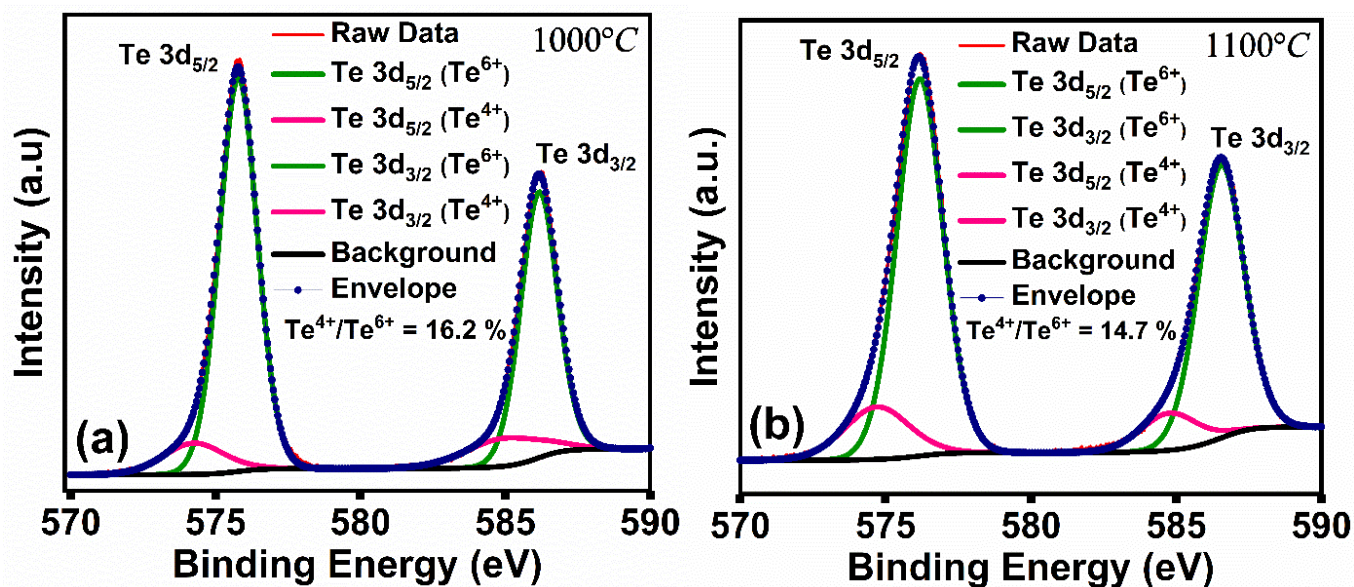

Fig. S10. High resolution XPS Te3d scan of BMTO annealed at (a) 1000ºC and (b) 1100ºC
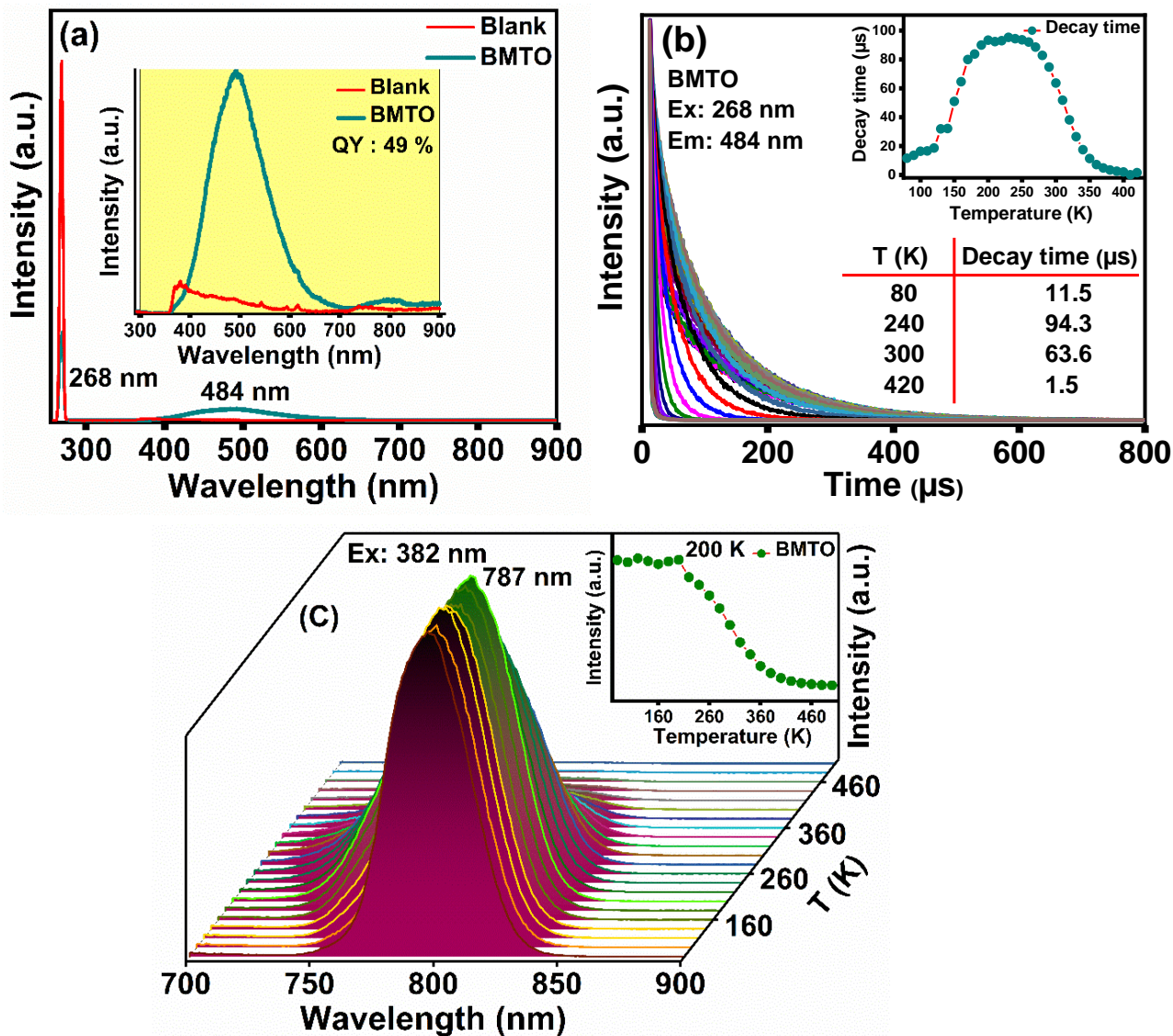
Fig. **S11**. (a) Quantum yield of BMTO under 268 nm excitation and 484 nm emission wavelength, (b) Temperature-dependent decay curve of BMTO under 268 nm excitation and 484 nm emission, (c) Temperature-dependent NIR emission of BMTO under 382 nm excitation.

In the present BMTO double perovskite system, the Eu^{3+} ions are intended to substitute the 12 coordinated A-site cations. The ionic radius of Mg^{2+} and Eu^{3+} ions were around 0.72 Å and 0.947 Å for coordination number (CN) 6, and the ionic radius of Ba^{2+} and Eu^{3+} ions were around 1.61 Å and 1.23 Å for CN=12.

Fig. S12. (a) XRD patterns of BMTO:x Eu^{3+}, (b) Raman spectra of BMTO:x Eu^{3+} (x = 0-0.09), (c)Rietveld refinement 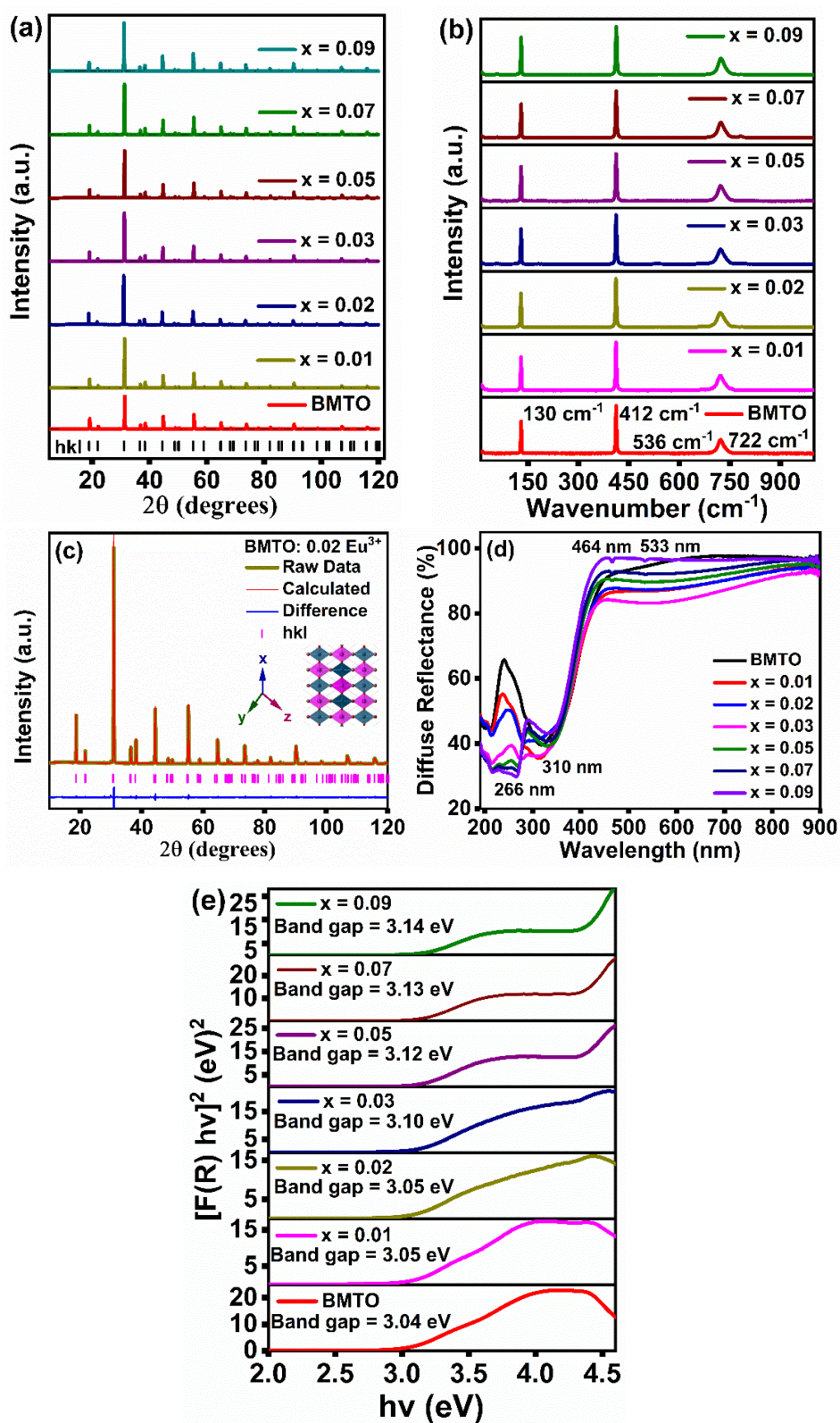of XRD pattern of BMTO:0.02 Eu^{3+}, (d) Diffuse reflectance of BMTO: x Eu^{3+} (x = 0 to 0.09), (e) Band gap energy of BMTO:x Eu^{3+} (x = 0 to 0.09) calculated using the Kubelka-Munk function.

The acceptable radius percentage difference is less than 30 % with respect to the equation 3.

$$Dr = \frac{Rs(CN) - Rd(CN)}{Rs(CN)} \times 100\ \%$$ (3)

Where R_s and R_d are the ionic radius of substituted and doped ions,[18] for Eu^{3+} ions, the Dr values are 23.6 % for Ba^{2+} and 31.52 % for Mg^{2+} respectively. Therefore, it is evident that Eu^{3+} ions could preferentially substitute the Ba^{2+} ions in the BMTO host lattice.

Fig. S12a. represents the XRD patterns of BMTO: x Eu^{3+}. XRD patterns of the doped samples were identical to that of the BMTO system, indicating a similar tetragonal structure ($I4/m$) for all the Eu^{3+} doped BMTO. All the diffraction patterns of the doped samples matched well with those of parent BMTO, and no impurity peaks were observed, which indicates that all the Eu^{3+} ions were successfully incorporated into the host crystal lattice without disturbing the crystal structure. To confirm the crystal structure, the refinement of BMTO: xEu^{3+} was done, and the Rietveld refinement of BMTO: $0.02Eu^{3+}$ was shown in Fig. 12c. The refined crystallographic and cell parameters of BMTO:$0.02Eu^{3+}$ were shown in In Table S4.

Table S4. Refined crystallographic and cell parameters of BMTO: 0.02 Eu^{3+}

Formula	: $Ba_{2-x}Eu_xMgTeO_6$					
Crystal system	: Tetragonal					
Space group	: $I4/m$					
Cell Parameters	: $a = b = 5.7487(0)$ Å, $c = 8.1151(8)$ Å, $V = 268.18$ Å^3					
Reliability factors	: $Rwp = 6.00\ \%$, $Rp = 4.31\ \%$, $GOF = 1.59$					
Atom	Site	x	y	z	Occupancy	Beq
Ba1	4d	0	0.5	0.25	0.99	1.9
Eu1	4d	0	0.5	0.25	0.01	1.9
Mg1	2a	0	0	0.5	1	1
Te1	2b	0	0	0	1	1
O1	4e	0.239	0.205	0	1	0.1
O2	8h	0	0	0.245	1	1

The lattice parameters and reliability factors after refinement of the XRD patterns of all the doped BMTO systems are shown in Table S5. The lattice parameters and the cell volume gradually decrease when the doping concentration increases from x=0 to x=0.09. This implies a lattice contraction with respect to the Eu^{3+} doping content, which is due to the substitution of Ba^{2+} by smaller Eu^{3+} ions.

Table S5. Refined lattice parameters and reliability factors of BMTO:x Eu^{3+} (x = 0-0.09)

Material	Lattice parameter (Å)	Cell volume (Å^3)	Rwp (%)	Rp (%)	GOF
Ba_2MgTeO_6	$a = b = 5.8235(0)$ $c = 8.1165(0)$	275.25	6.22	4.37	1.72
Ba_2MgTeO_6: 0.01 Eu^{3+}	$a = b = 5.7522(3)$ $c = 8.1263(5)$	268.88	6.75	4.32	1.76
Ba_2MgTeO_6: 0.02 Eu^{3+}	$a = b = 5.7518(1)$ $c = 8.1193(1)$	268.61	6.00	4.31	1.59
Ba_2MgTeO_6: 0.03 Eu^{3+}	$a = b = 5.7442(5)$ $c = 8.1381(6)$	268.53	5.54	4.02	1.42
Ba_2MgTeO_6: 0.05 Eu^{3+}	$a = b = 5.7499(8)$ $c = 8.1203(7)$	268.47	6.23	4.63	1.66
Ba_2MgTeO_6: 0.07 Eu^{3+}	$a = b = 5.7453(9)$ $c = 8.1175(5)$	267.95	6.24	4.29	1.52
Ba_2MgTeO_6: 0.09 Eu^{3+}	$a = b = 5.7450(8)$ $c = 8.1172(0)$	267.91	6.85	4.63	1.80

The crystal structure is again confirmed by analyzing the Raman spectra. Fig. S12b shows the Raman spectra of BMTO: x Eu^{3+}. The similar Raman spectral profiles of BMTO and Eu^{3+} doped BMTO have indicated a similar structure for all the materials. The modes in the host system were also present in the Eu^{3+} substituted samples, confirming that the Eu^{3+} ions were successfully incorporated within the BMTO matrix without disturbing its crystal structure. The dominant bands present in the parent and Eu^{3+} doped samples were shown in Fig. S12b, where the mode present at 130 cm^{-1} represents the external mode $T_{2g}(1)$. The modes at 436, 536, and 722 cm^{-1} correspond to the internal modes v_5, v_2, and v_1, respectively. Further, the diffuse reflectance of BMTO: x Eu^{3+} (x=0 to 0.09) was measured and is shown in Fig. S12d.[19] It is noted that all the Eu^{3+} doped materials exhibit absorption in the UV region. The absorption at 464 nm and 533 nm are due to the characteristic absorptions of Eu^{3+} ions. The band gap of the materials was calculated using the Kubelka-Munk function and is shown in Fig. S12e.[20-22] The direct band gap increases (3.0 to 3.1 eV, small increment) with respect to the substitution of

Eu^{3+} ions. The substitution of smaller Eu^{3+} ions might lead to a decrease in conduction band width and thereby cause an increase in band gap energies of Eu^{3+} substituted BMTO materials. An increase in band gap energy with respect to the A-site substitution is also observed in ALaLiTeO$_6$ (A= Sr, Ba) and A$_2$MTaO$_6$ (A= Ba, Sr, La B= Y, Al, Li) double perovskite systems.[23,24] Fig. S13a depicts the photoluminescence excitation and emission spectra of 0.02 Eu^{3+} activated BMTO system. The excitation band centered at 268 nm corresponds to the $^1A_{1g}$ → $^3T_{2u}$ transitions of Te^{4+} in the BMTO system. The emission band includes the unusual host emission at 484 nm and the characteristic emissions of Eu^{3+} ions. The broad emission at 484 nm is due to the $^3T_{2u}$, $^3T_{1u}$ → $^1A_{1g}$ transitions of Te^{4+} ions, and the dominant emission centered at 595 nm is due to the $^5D_0$ → $^7F_1$ magnetic dipole transitions of Eu^{3+} ions. Also, a less intense arrow emission band was observed at 613 nm, which is due to the characteristic $^5D_0$ → $^7F_2$ electric dipole transitions of Eu^{3+} ions. This is the first time a broad emission and an intense orange emission are observed in the tellurate-based double perovskite system activated with Eu^{3+} ions.

The excitation and emission spectra monitored at 613 nm emission wavelength and 360 nm excitation wavelength are shown in Fig. S13b. The excitation spectra contain broad bands centered at 268 nm and 360 nm. The band at 268 nm corresponds to the absorptions of Te^{4+} ions, and the band at 360 nm is attributed to the overlap of host absorption and Eu^{3+}- O^{2-} charge transfer band in BMTO.
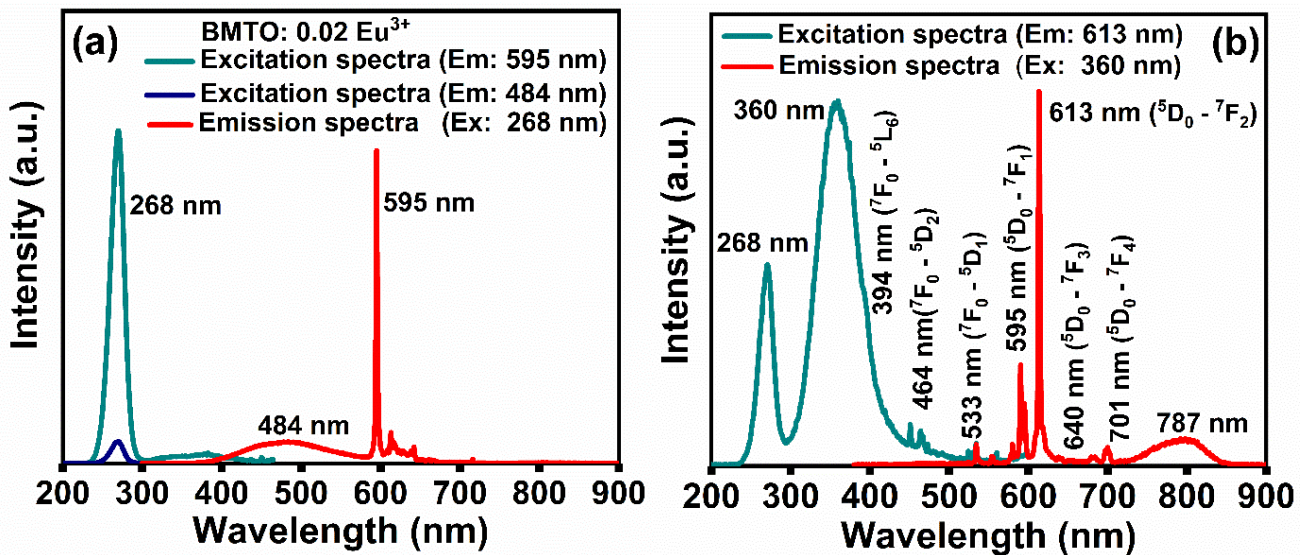

Fig. S13. (a) Photoluminescence excitation and emission spectra of BMTO: 0.02 Eu^{3+}, (b) The excitation and emission spectra of BMTO: 0.02 Eu^{3+} monitored at 613 nm emission wavelength and 360 nm excitation wavelength.

The presence of charge transfer band (CTB) in the UV region is common in Eu^{3+} doped phosphors and is originates from the O^{2-} - Eu^{3+} charge transfer transition. A broad excitation band between 200 - 350 nm was previously reported in Eu^{3+}-activated $LaBMoO_6$ which is attributed to the overlap of MoO^5 group absorption and O^{2-} –Eu^{3+} charge-transfer state (CTS) band.[25] Another double perovskite La_2MgZrO_6: Eu^{3+} exhibit broadband absorption in the 250 - 350 nm region which originates from the charge transfer band (CTB) from the O^{2-} to Eu^{3+} ions.[26] A weak CTB of O^{2-} -Eu^{3+} was observed in the near UV region (250 – 350 nm) for La_2WO_6: Eu^{3+} phosphor.[27] Sr_2MgTeO_6: Eu^{3+} and Ca_2MgTeO_6: Eu^{3+} are similar systems when compared to the Ba_2MgTeO_6 system and it exhibit wide excitation band between 230 – 330 nm and is attributed to the charge transfer band of O^{2-} to Eu^{3+}.[28,29] Hence it is confirmed that the O^{2-} - Eu^{3+} CT band is very common in Eu^{3+} doped oxide phosphors. It is also noted that host BMTO exhibit absorption in the 300 – 500 region. While monitoring the emission at 627 nm the host excitation maxima is located at 340 nm and while monitoring the emission at 787 nm the host excitation maxima is located at 382 nm which is shown in the Fig. 1 e – f. Thus it is confirmed that host BMTO exhibit wide absorption band in the 300 – 450 region. Hence the wide excitation band present in BMTO: Eu^{3+} system exhibit as shown in Fig. S13b can be attributed to the overlap of host absorption and O^{2-} - Eu^{3+} charge transfer band in BMTO: Eu^{3+}. The characteristic absorption peaks due to the intra *4f-4f* transitions of Eu^{3+} ions are also observed and is marked in the Fig. S13b. A shoulder peak around 394 nm is noted which is attributed to the $^7F_0$ – $^5L_6$ electronic transition of Eu^{3+} ions. Other excitation peaks located at 464 ($^7F_0$ – $^5D_2$) and 533 nm ($^7F_0$ – $^5D_1$) are also originating from the inner *4f-4f* transitions of Eu^{3+} ions. The intensity of Eu^{3+} typical *4f-4f* transitions were lower when compared to the intensity of broad excitation band around 360 nm. The absence of other excitation peaks of Eu^{3+} ions may be due to their low intensity or the overlapping of such excitation peaks with the broad excitation band.

The emission lines observed were due to the characteristic $^5D_0 \rightarrow {^7F_J}_{(J=1,2,3\ \&\ 4)}$ transitions of Eu^{3+} ions, and the highly intense red emission observed at 613 nm is ascribed to the $^5D_0 \rightarrow {^7F_2}$ electric dipole transitions of Eu^{3+} ions.[18,19,30] A broad emission band centered at 787 nm was also observed and is due to the $^3A_{1u}$, $^3T_{1u} \rightarrow {^1A_{1g}}$ transitions Te^{4+} ions within the BMTO system.

The PL emission spectra at each concentration under different excitations (360 nm, 395 nm, 464 nm, and 532 nm) were recorded and are shown in Fig. S14a-d. Among them, emission under 360 nm excitation is the dominant one, and the intensity of 613 nm emission under each excitation increases with respect to the Eu^{3+} doping content. Here, the emission intensity does not decline even at x= 0.13. This might be due to the fact that the quenching concentration may come beyond x = 0.13. Some of the phosphors doped with Eu^{3+} were previously reported with quenching at higher concentrations, and some of them reported with non-quenching nature even at higher concentrations. The red emission under 360, 395, 464, and 532 nm excitations is beyond the scope of our study, we focus more on the dual emissive nature of BMTO under 268 nm excitation.

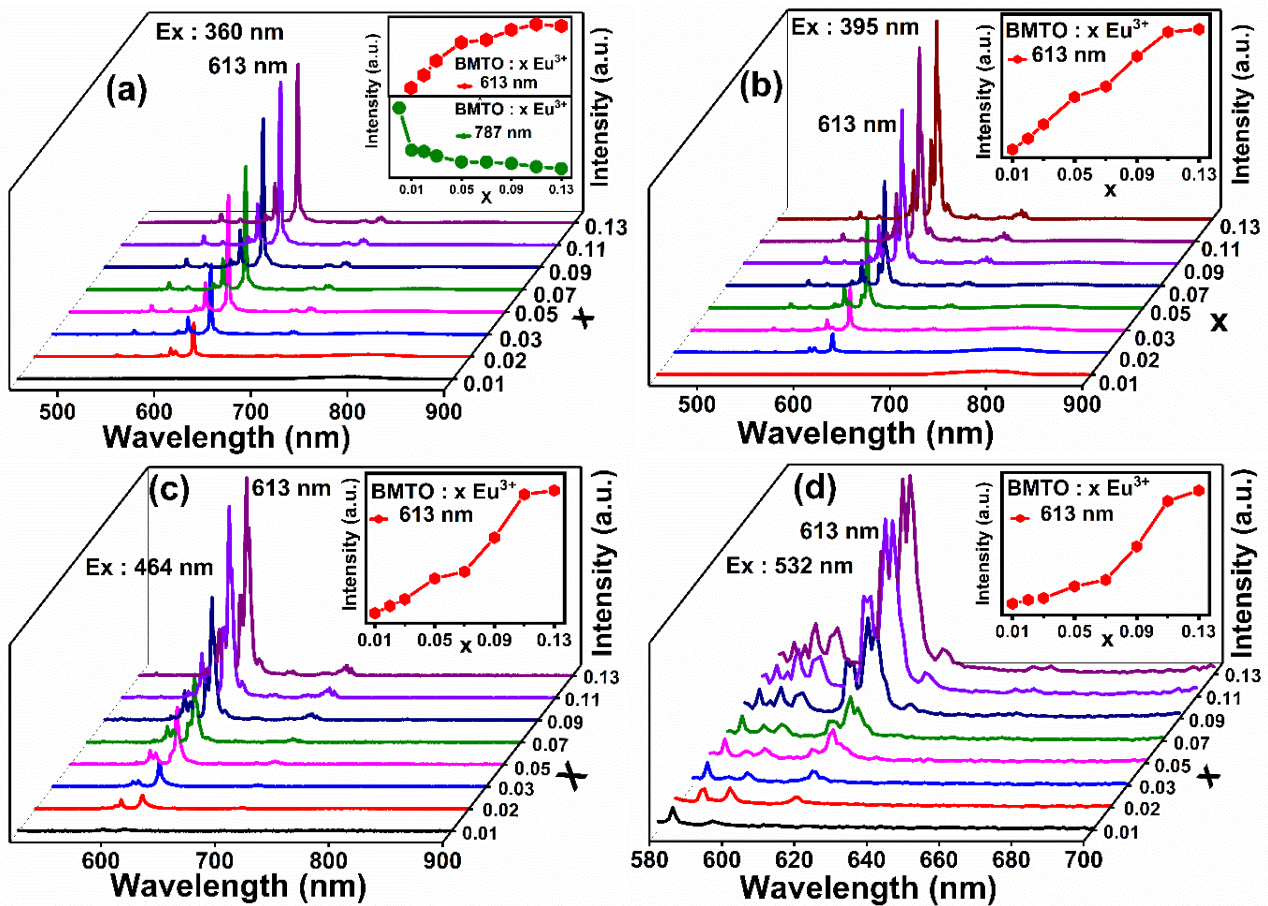**Fig. S14.** BMTO:xEu^{3+} under (a) 360nm, (b) 395 nm, (c) 464 nm, (d) 532 nm excitations.

Further, the emission properties at different excitations with respect to each concentration were studied (Fig. S15 and S16).
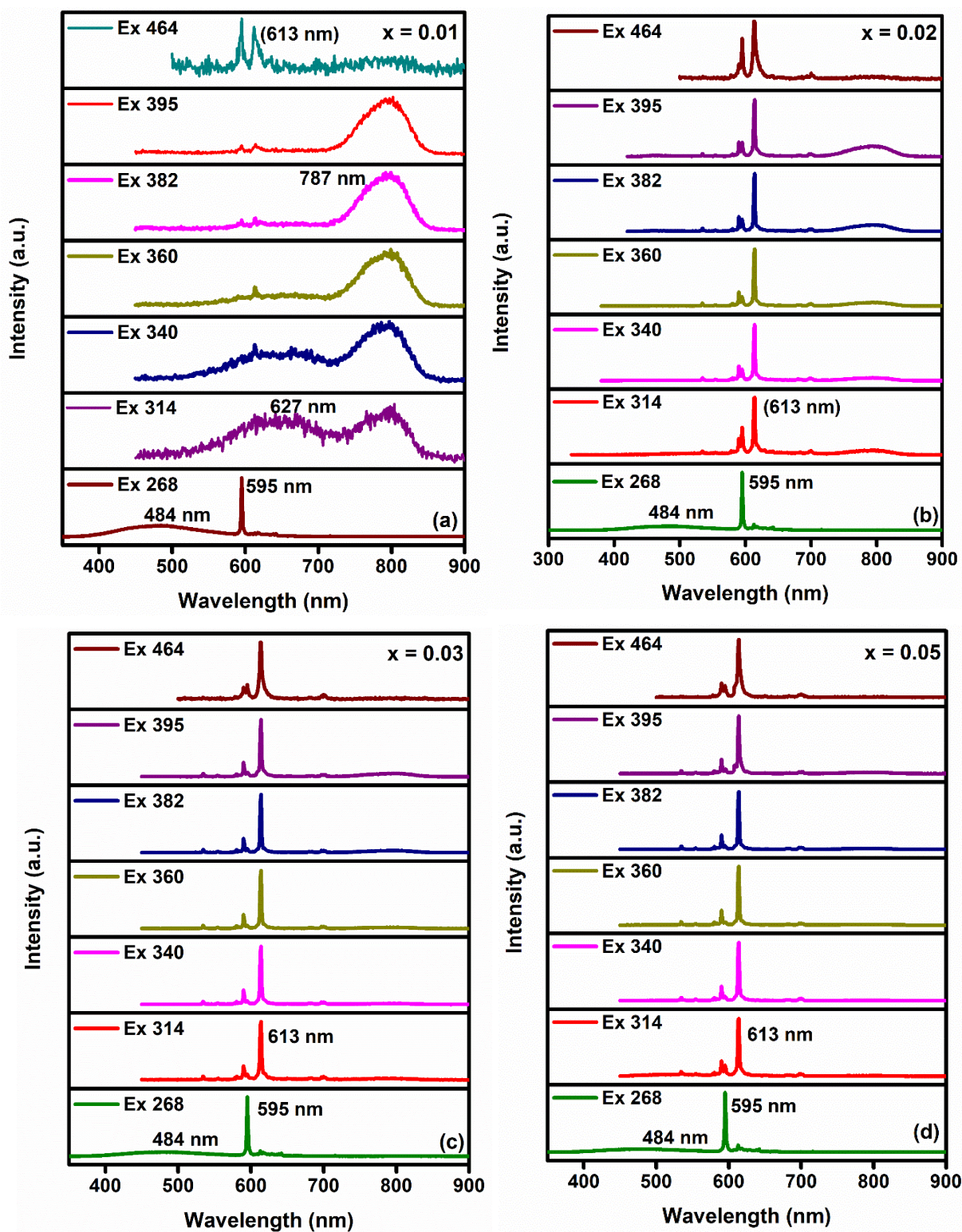

Fig. S15. Photoluminescence spectra of BMTO: x Eu^{3+} at different excitation. (a) x = 0.01, (b) x = 0.02, (c) x = 0.03, (d) x = 0.05.
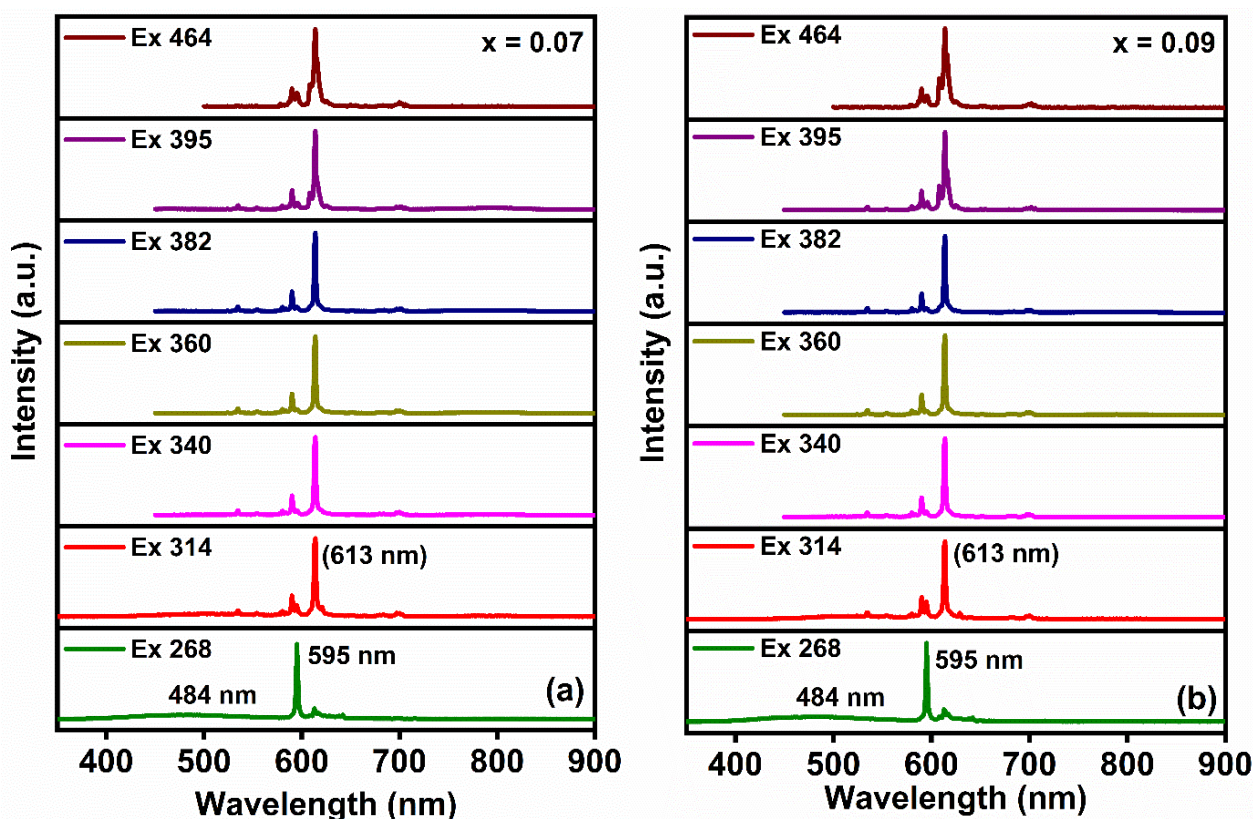
Fig. S16. Photoluminescence spectra of BMTO: x Eu^{3+} at different excitation. (a) x = 0.07, (b) x = 0.09.

The variation of emission intensity at 595 and 613 nm under 268, 360, and 395 nm excitations was shown in Fig. S17a-c. For every concentration, the orange emission is dominant under the excitation of 268 nm, while the red emission is dominant for other excitations. Under 268 nm excitation, magnetic dipole transition is favored over electric dipole transition. Moreover, the tuning of emission from orange to red with respect to the excitation wavelength depends upon the substitution site of Eu^{3+} ions in the host system. So the dopant Eu^{3+} ions can be a very sensitive tool to probe the local symmetry of the system.

Generally, magnetic dipole transition is favored when the Eu^{3+} ions occupy a crystallographic site with inversion symmetry, and electric dipole transition is favored when the Eu^{3+} ions occupy a non-centrosymmetric site. The switching between orange and red emissions under different excitations is not a general case and is analyzed in terms of asymmetry ratio. The

occupation site of Eu^{3+} ions can be obtained by calculating the asymmetry ratio ($^5D_0 \rightarrow {}^7F_2/{}^5D_0 \rightarrow {}^7F_1$), and the ratio greater than one indicates an A –site occupation of Eu^{3+} ions.
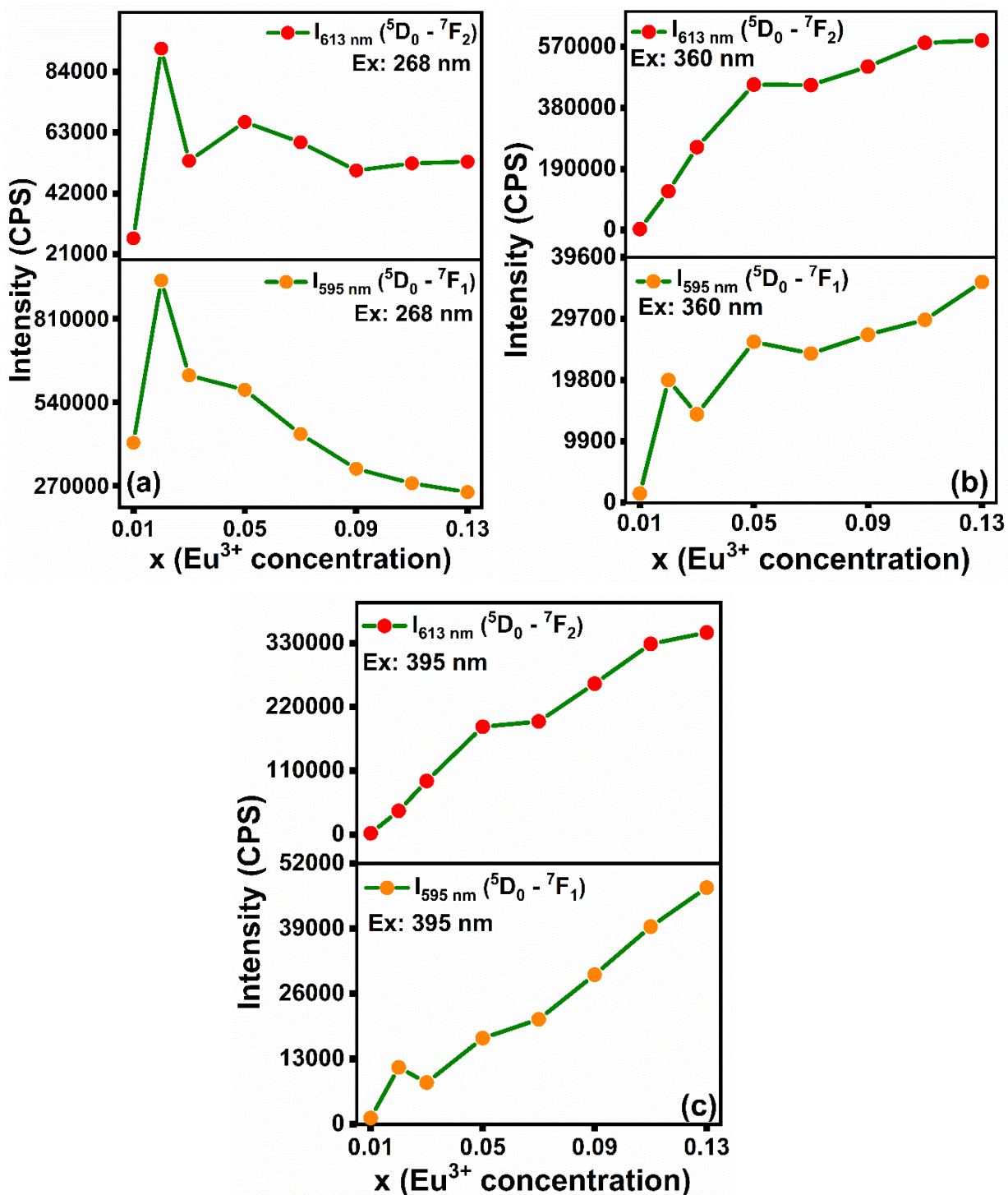

Fig. S17. Variation of emission intensity at 595 and 613 nm of BMTO: x Eu^{3+} with the doping concentration x under (a) 268 nm, (h) 360 nm and (c) 395 nm excitations.

Table S6. Asymmetry ratio of BMTO:x Eu^{3+} under different excitations.

Concentration (x)	Asymmetry ratio ($I_{613}I_{595}$)				
	Ex: 268 nm	Ex: 360 nm	EX: 395 nm	Ex: 464 nm	Ex: 532 nm
0.01	0.06	1.88	1.10	0.70	0.55
0.02	0.09	6.03	3.94	1.38	0.58
0.03	0.08	18.26	12.59	3.60	1.03
0.05	0.11	18.54	12.73	4.68	2.04
0.07	0.13	20.58	12.42	5.27	2.42
0.09	0.15	19.87	11.33	6.47	3.85
0.11	0.18	19.78	10.69	6.5	4.48
0.13	0.20	17.09	9.93	6.76	4.65

Table S7. Refined lattice parameters and reliability factors of BMTO: x Eu^{3+} (x = 0-0.09) by considering the partial substitution of Eu^{3+} ions.

Material	Lattice parameter (Å)	Cell volume (Å^3)	*Rwp* (%)	*Rp* (%)	*GOF*
Ba_2MgTeO_6	$a = b = 5.8235(0)$ $c = 8.1165(0)$	275.25	6.22	4.37	1.72
Ba_2MgTeO_6: 0.01 Eu^{3+}	$a = b = 5.7493(5)$ $c = 8.1210(9)$	268.44	7.11	4.71	1.86
Ba_2MgTeO_6: 0.02 Eu^{3+}	$a = b = 5.7498(4)$ $c = 8.1163(1)$	268.33	6..20	4.34	1.65
Ba_2MgTeO_6: 0.03 Eu^{3+}	$a = b = 5.7488(1)$ $c = 8.1176(0)$	268.27	5.77	4.28	1.48
Ba_2MgTeO_6: 0.05 Eu^{3+}	$a = b = 5.7354(0)$ $c = 8.1244(4)$	267.25	6.33	4.52	1.68
Ba_2MgTeO_6: 0.07 Eu^{3+}	$a = b = 5.7457(0)$ $c = 8.1143(1)$	268.08	6.61	4.68	1.60
Ba_2MgTeO_6: 0.09 Eu^{3+}	$a = b = 5.7419(4)$ $c = 8.1143(1)$	267.52	6.92	4.58	1.83

Since BMTO exhibit intense orange and red light under different excitations, the photophysical response of BMTO: 0.02 Eu^{3+} under both 268 and 360 nm excitation were studied. It is observed that the emission intensity is very much dominant under 268 nm excitation than 360 nm excitation and is shown in Fig. S18b. Further the quantum yield under both 268 and 360 nm excitation was measured and the best quantum yield was obtained under 268 nm excitation and is shown in Fig S18c-d.
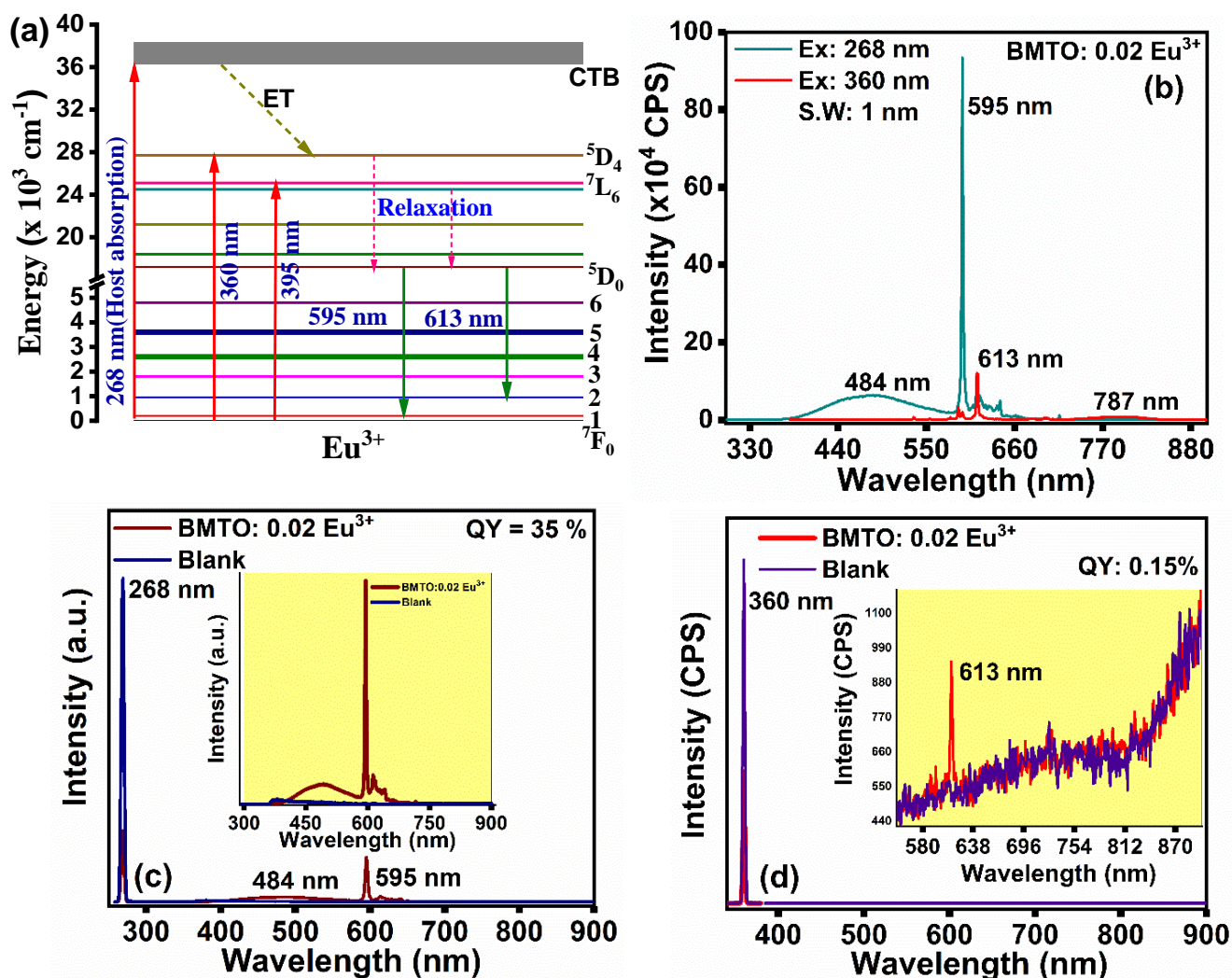
Fig. S18. a) Schematic representation of energy transfer from host to Eu^{3+} ions, (b) PL emission spectra of BMTO: 0.02 Eu^{3+} under 268 and 360 nm excitation wavelength, (c) Quantum yield of BMTO:0.02 Eu^{3+} under 268 nm excitation, (d) Quantum yield of BMTO:0.02 Eu^{3+} under 360 nm excitation.

A quantum yield of 35% was obtained under 268 nm excitation which is much higher than that under 360 nm (0.15%) excitation. Also it is noted that the inherent cyan emission and the

characteristic Eu^{3+} emission is visible under 268 nm excitation than 360 nm excitation and this can be effectively used for optical thermometry. Since the better luminescence performance and quantum yield was obtained under 268 nm excitation, the current study focused more on the luminescence of BMTO: 0.02 Eu^{3+} with respect to the 268 nm excitation for temperature sensing applications.
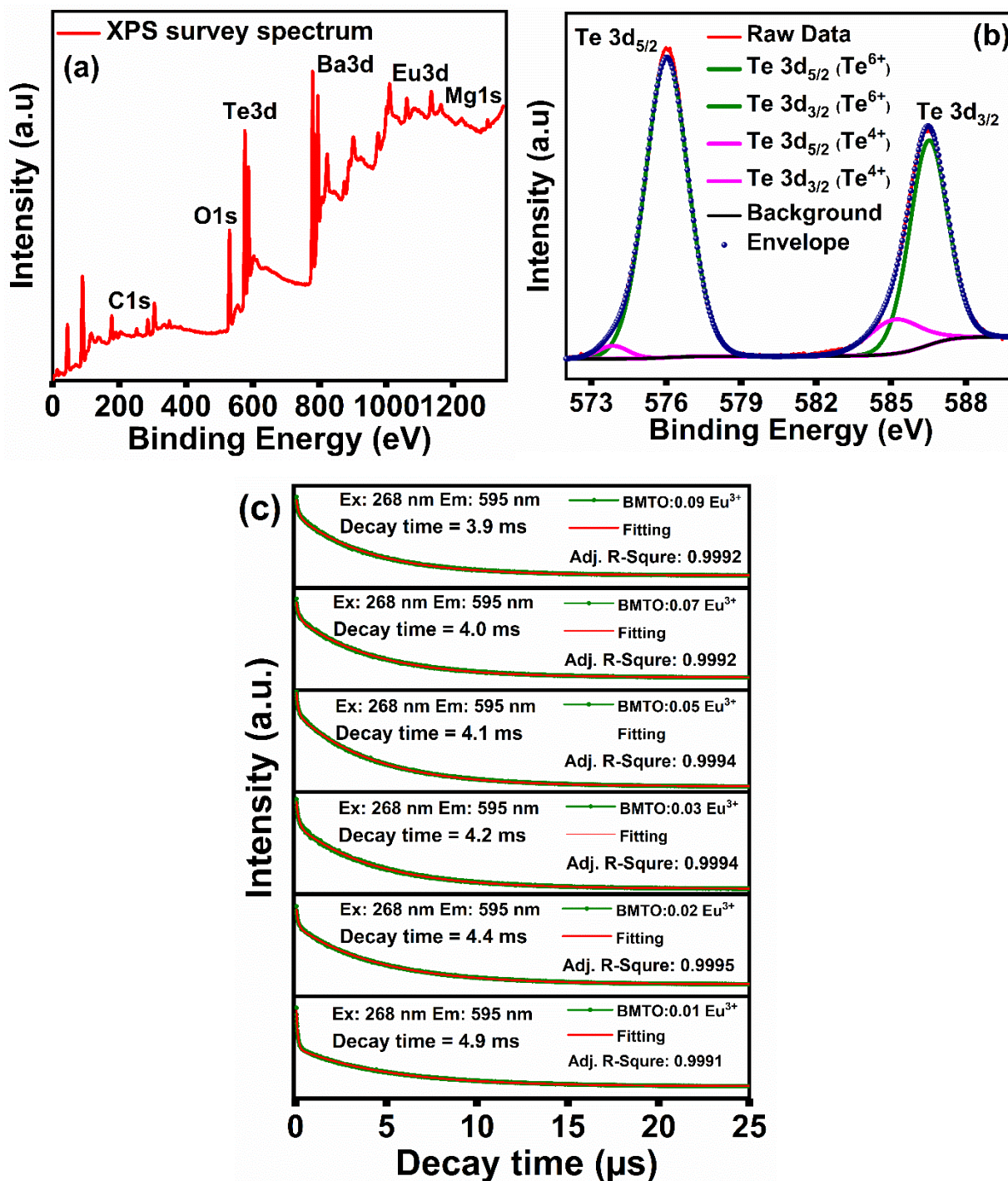

Fig. S19. a) XPS survey spectrum of BMTO:0.02 Eu^{3+}, (b) High-resolution XPS spectra for Te3d scan, (c) Decay curves of BMTO: xEu^{3+} monitored under 595 nm emission wavelength.

To confirm the presence of Te^{4+} ions in the Eu^{3+} activated system, XPS analysis was carried out on BMTO: 0.02 Eu^{3+} material. The survey spectrum and high-resolution Te3d scan of the x=0.02 sample are shown in Fig. S19a-b. The survey spectrum confirms the presence of all the elemental components in the BMTO:0.02 Eu^{3+} material. The amount of Te^{4+} ions can be estimated by the careful fitting of a high-resolution *3d* scan of BMTO:0.02 Eu^{3+}.

Using McCamy method, the correlated color temperature (*CCT*) can be calculated using the equation 4,[31]

$$CCT + -449n^3 + 3525 \ n^2 - 6823.3n + 5520.33 \tag{4}$$

Where, $n = (x\text{-}xe/y\text{-}ye)$, (x, y) is the CIE coordinates and $(x_e\text{-}y_e)$ is a constant (0.3320, 0.1858). The calculated color temperature is 5095 K which ensures a cool light for the phosphor material. The critical concentration of the Eu^{3+} ions were obtained as x = 0.02 beyond which concentration quenching happens. At higher concentrations, the non-radiative energy transfer among Eu^{3+} ions increases and correspondingly, the emission intensity decreases. According to Blasse, the critical energy distance is approximately equals to twice the radias of a sphere with the volume of corresponding unit cell. So the critical distance (R_c) for the energy transfer between the Eu^{3+} ions can be calculated using the Blasse equation.[18,19]

$$Rc \approx 2(3V|4\pi XcN)^{1/3} \tag{5}$$

Where, V, X_c and N represent the volume of the unit cell, critical concentration and the number of host cations in the unit cell respectively. Taking the values of V (268.61 $Å^3$), X_c (0.02) and N (2), the critical energy distance (Rc) was estimated to be 23.4 Å which is greater than 4 Å implies an electric multipolar interaction among the activators ions in the BMTO matrix. Thus the type of energy transfer can be quantitatively explained using the Dexter's equation 6.[18]

$$\frac{I}{x} = k\left[1 + \beta(x)^{\theta/3}\right]^{-1} \tag{6}$$

Where I is the luminescence intensity, x is the concentration, k and β are the constants for a typical system and θ is the multipolar interaction constant in which $\theta = 3, 6, 8$ and 10 corresponds to exchange interaction, dipole – dipole (*d-d*) interactions, dipole – quadrupole (*d-q*) and quadrupole – quadrupole interactions (*q-q*), respectively. From the plot of log(I/x) vs log (x) as shown in Fig. S20, θ value can be estimated. From the slope parameter, the θ value is obtained as 4.86 which are closer to 6, indicating that the dipole-dipole interaction was the major reason for concentration quenching.
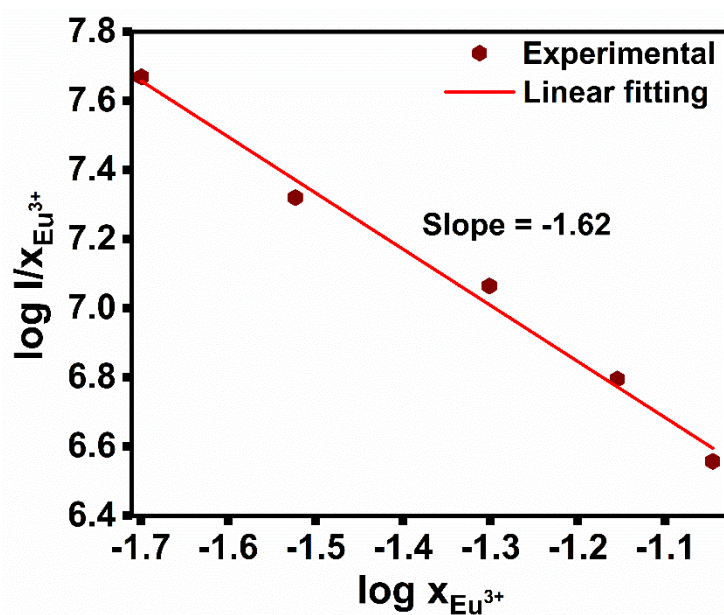
FIG. S20. The log (I/x) – log(x) diagram of BMTO: x Eu^{3+} phosphors

Table S8. Variation of CIE coordinates of BMTO:0.02 Eu^{3+} with the temperature

Temperature (K)	CIE Coordinates (x,y)
300	(0.39, 0.33)
310	(0.40, 0.33)
320	(0.42, 0.34)
330	(0.45, 0.34)
340	(0.48, 0.34)
350	(0.50, 0.35)
360	(0.52, 0.35)
370	(0.54, 0.35)
380	(0.55, 0.36)
390	(0.55, 0.36)
400	(0.56, 0.36)
420	(0.56, 0.36)
440	(0.56, 0.36)
460	(0.56, 0.36)
480	(0.55, 0.37)
500	(0.55, 0.38)

Calculation of radiative and non radiative decay rates using Judd-Ofeltintensity theory

The radiative and non radiative decay rates of BMTO:0.02Eu^{3+} at various temperatures were calculated from the emission spectra using *4f-4f* intensity theory. By this theory, the magnetic dipole ($^5D_0 \rightarrow {}^7F_1$) transition rate of Eu^{3+} ion (A_{01}) is given by,[31-33]

$$A_{01} = \frac{64\pi^4 \vartheta_1^3 n^3 S_{md}}{3J\,(2J+1)} \tag{7}$$

Where, A_{01} is the Einstein coefficient between $^5D_0$ and $^7F_1$ levels, v_1 is the wave number of magnetic dipole transition, n is the effective refractive index of the BMTO, $S_{md} = 7.83 \times 10^{-42}$ (constant independent of the medium) and h is the planks constant ($h=6.6261\times10^{-34}$Js). For $^5D_0$ transitions $2J+1$ equal to 1.

The electric dipole transition rate, A_{0J} (*J*=2, 4 and 6) is given by,

$$A_{0J} = \frac{64\pi^4 v_J^3}{3h\,(2J+1)} e^2 \frac{n(n^2+2)^2}{9} \sum_{\lambda=2,4,6} \Omega_\lambda <^5 D\|U^{(\lambda)}\|^7 F_J >^2 \tag{8}$$

Where A_{0J} is the coefficient of spontaneous emission, Ω_λ is Judd-Ofelt intensity parameter and e is the electronic charge. The squared reduced matrix element $<^5 D\|U^{(\lambda)}\|^7 F_J >^2$ have values 0.00324, 0.00229 and 0.00023 for *J*=2, 4 and 6 respectively. The sum of radiative rates (A_{0J}) for each $^5D_0$-^7F_J transition gives the total radiative decay rate (A_R)

$$A_R = \sum A_{0J} = A_{01} \frac{v_{01}}{I_{01}} \sum_{J=2,4} \frac{I_{0J}}{v_{0J}} \tag{9}$$

Where v_{01}, v_{0J}, I_{01} and I_{0J} are the frequencies and the integrated emission intensities of $^5D_0 \rightarrow$ $^7F_1$ and $^5D_0 \rightarrow {}^7F_J$ transitions respectively. The non radiative decay rate A_{NR} is calculated by using the observed lifetime τobs with the relation,

$$A_{NR} = \frac{1}{\tau_{obs}} - A_R$$

Table S9. Radiative (A_R) andnon radiative (A_{NR}) decay rates of BMTO:0.02Eu^{3+} at different temperatures.

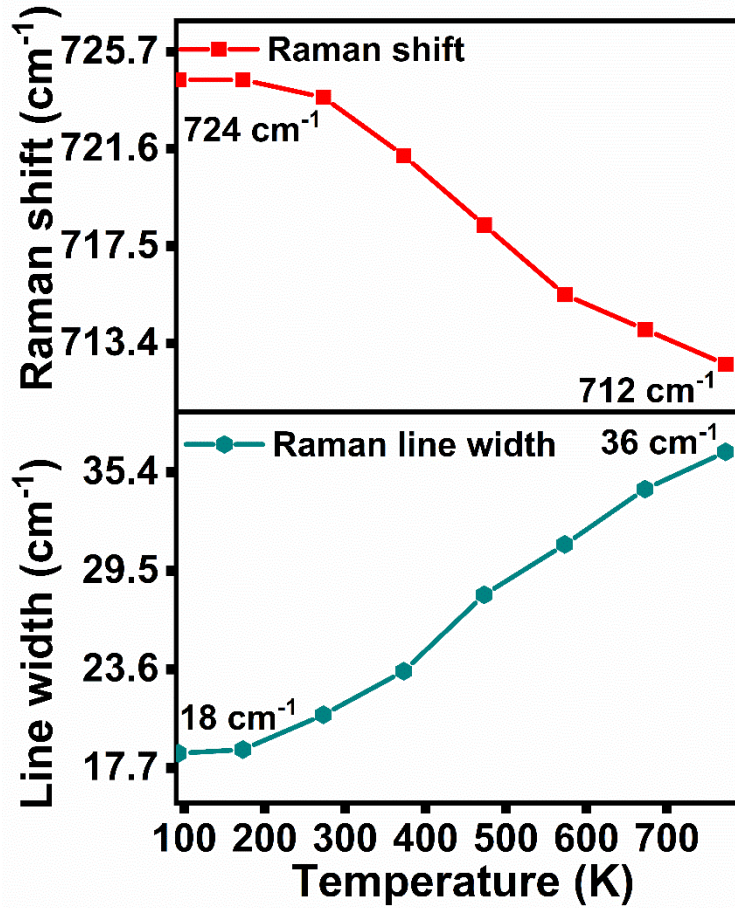| Temperature [K]	τ_{obs} [ms]	A_R [s^{-1}]	A_{NR} [s^{-1}]
80	4.73	131	79
120	4.61	132	84
180	4.42	139	86
240	4.17	148	91
300	3.95	153	99
360	3.92	153	102
420	3.52	154	129

Fig. S21. The variation in Raman shift and Raman line width with respect to temperature.

Optical temperature sensing of BMTO: 0.02 Eu^{3+}

The relative sensitivity is calculated using the equation 11,[34-37]

$$Sr \text{ (\%/K} = \left| \frac{1}{Q} \frac{\partial Q}{\partial T} \right| \cdot 100 \text{ \%} \tag{11}$$

Where Q is an indication, which can be fluorescence intensity ratio (*FIR*), excitation intensity ratio (*EIR*), line shift, line broadening, lifetime, etc. Relative sensitivity is an important parameter in the case of temperature sensors and is defined as the relative change in the *FIR* parameter per degree of temperature change (%/K).

Fluorescent intensity ratio (FIR) mode

Based on the FIR mode, the relative sensitivity S$_r$ is calculated by using the equation 12,[38,39]

$$S_r = 100 \times \frac{1}{FIR} \frac{\partial FIR}{\partial T} \text{ \%/K} \tag{12}$$

The fluorescence intensity ratios of I_{595}/I_{484} and I_{613}/I_{595} were used for the calculation of relative sensitivity S_r. The obtained *FIR* values were well-fitted by using the function,

$$FIR = A + B * EXP \text{ (-E/T)} \tag{13}$$

Where A, B, and E are constants, and T is the temperature. The fluorescence intensity of $^5D_0 \rightarrow {}^7F_2$ and $^5D_0 \rightarrow {}^7F_1$ transitions are first used for the FIR calculation, and the corresponding FIR vs Temperature plot is shown in Fig. S22a. The FIR values were well fitted by the function $A+B*EXP(-E/T)$ from 100 to 300 K, and the obtained Sr values were shown in Fig. S22b.
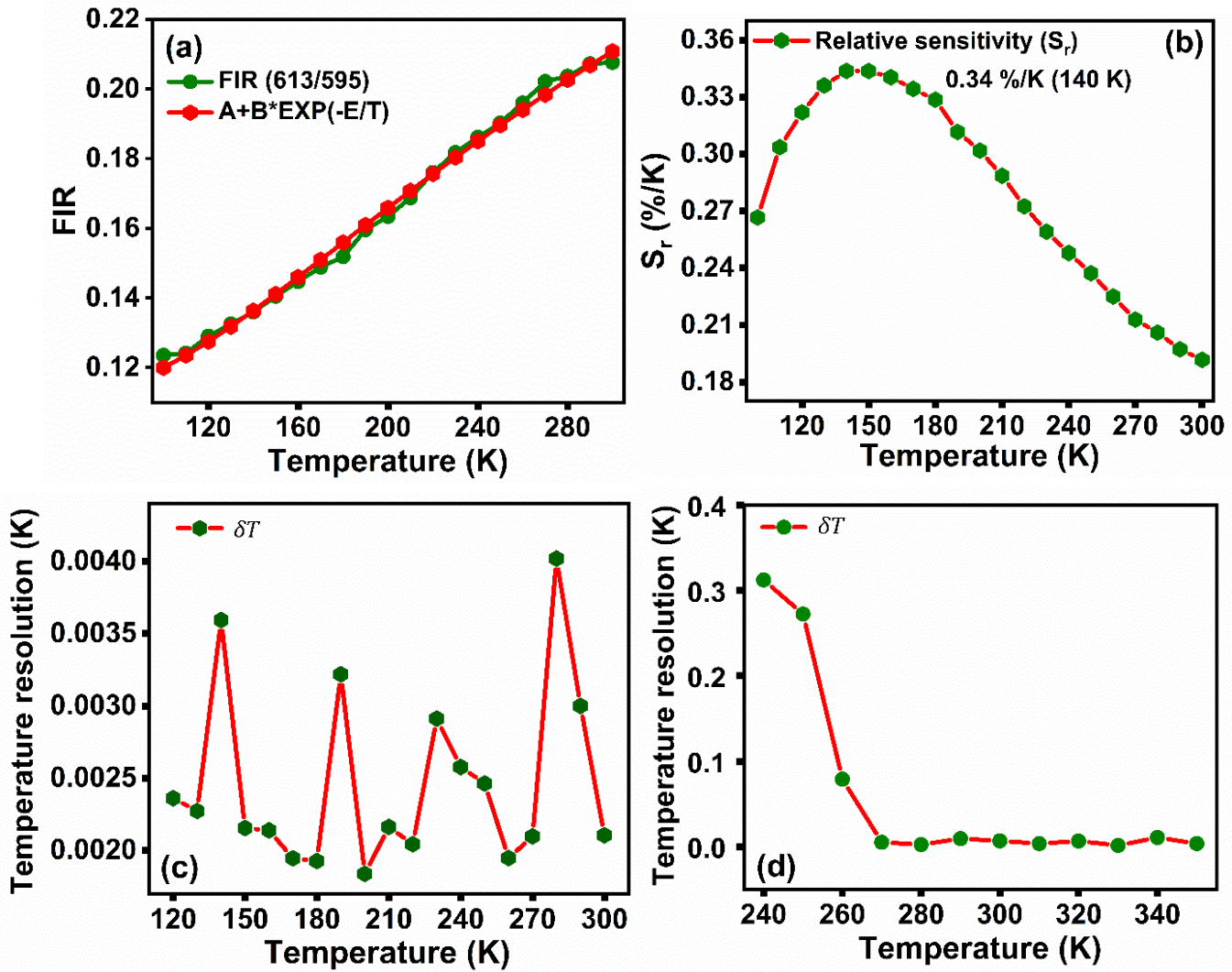
Fig. S22 (a) FIR based on I_{613}/I_{595} vs Temperature plot, (b) S_r based on I_{613}/I_{595} vs Temperature plot, (c) δT vs Temperature plot based $I_{613}/I_{595,}$ (d) δT vs Temperature plot based $I_{595}/I_{484,}$

Here, a maximum sensitivity of 0.34 %/K was obtained at 140 K.

Further, the temperature resolution (δT) is calculated usimg the following equation 14.

$$\delta T = \frac{1}{Sr}\frac{\delta FIR}{FIR} \tag{14}$$

where $\delta FIR/FIR$ is the relative error in the measurement. δT versus T graph based on I_{613}/I_{595} and I_{595}/I_{484} ratio is shown in Fig. S18c-d.

Line broadening

As the temperature increases, it is noted that the line width of the $^5D_0 \rightarrow {}^7F_1$ and $^5D_0 \rightarrow {}^7F_2$ transition increases homogeneously, which is the direct consequence of the interaction of Eu^{3+} ions with the phonons. The full width at half maximum (*FWHM*) of emission bands at 595 nm and 613 nm were adequately fitted with the function *A+B*EXP(-E/T)* as shown in Fig. S23a-b. where *A*, *B* and *E* are constants and *T* is the temperature.
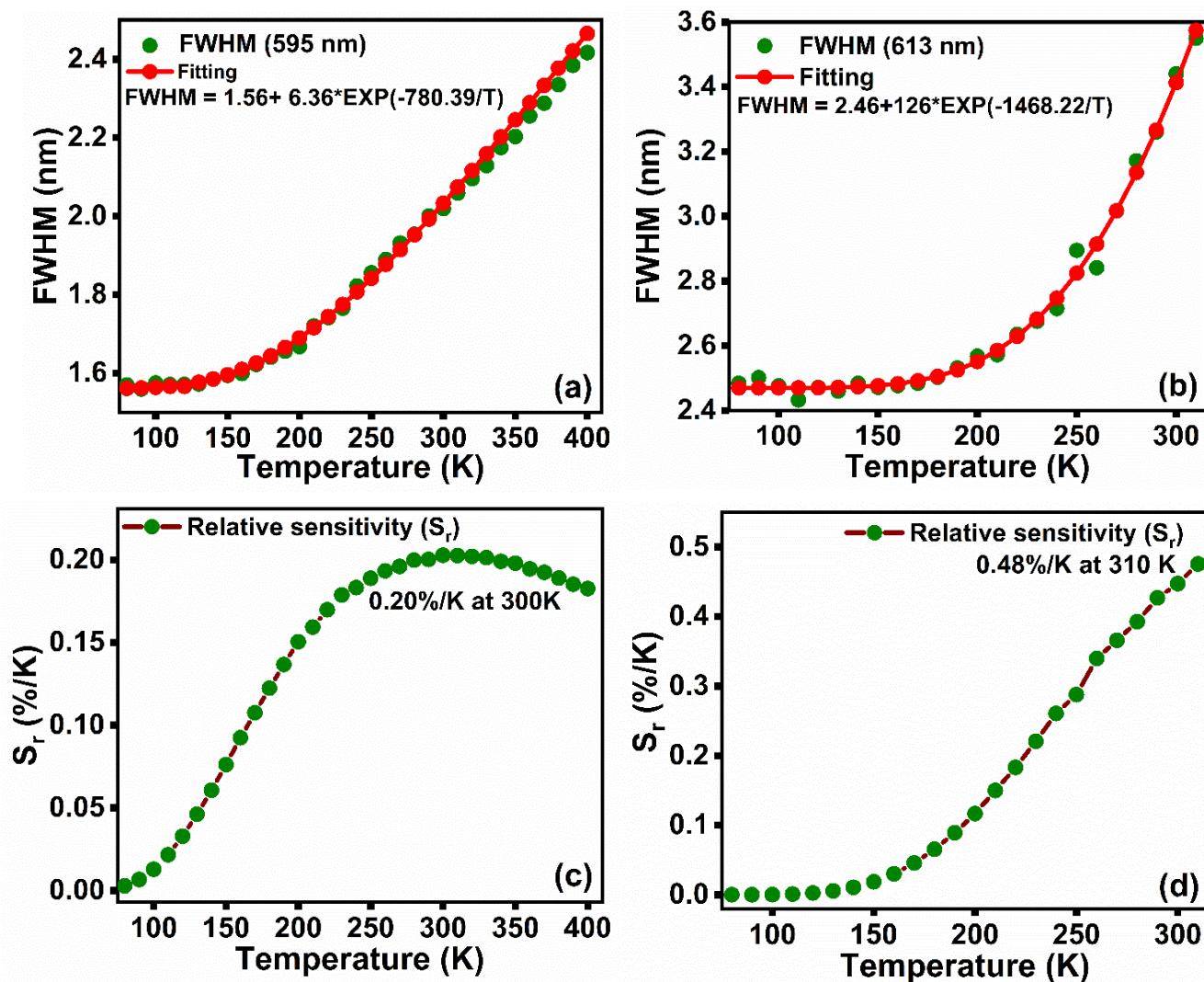
Fig. S23 (a) *FWHM* of 595 nm emission vs Temperature plot, (b) *FWHM* of 613 nm emission vs Temperature plot, (c) *Sr* based on FWHM (595 nm) vs Temperature plot, (d) *Sr* based on FWHM (613 nm) vs Temperature plot.

A maximum relative sensitivity of about 0.20 %/K at 300 K and 0.48 %/K at 310 K was obtained for $^5D_0 \rightarrow {}^7F_1$ and $^5D_0 \rightarrow {}^7F_2$ line broadening, respectively, and is shown in Fig. S23c-d.

Excitation intensity ratio of absorption edge (274 nm) to absorption at 268 nm

The anti-thermal quenching behavior of the excitation band at 268 nm and absorption edge at 274 nm in the excitation spectra of BMTO: 0.02 Eu^{3+} over the low-temperature region makes this method very effective for temperature sensing applications. Fig. S24a shows the enlarged portion of temperature-dependent excitation spectra and the variation of excitation intensity at 268 nm and 274 nm with respect to the temperature. Zhou et al., Duan et al., and recently Sariga et al. observed similar anti-thermal quenching behavior at the absorption edge of their excitation spectra in $GdVO_4$: Sm^{3+}, $LuVO_4$: Eu^{3+} and $SrLaLiTeO_6$: Eu^{3+} systems respectively.[36,40,41] The thermally populated ground state vibronic sublevels cause the redshift and the unusual negative quenching behavior in the excitation spectra. As the vibronic sublevels at the ground electronic state get populated with the temperature, more electrons with lesser energy will excited to the higher energy levels. The thermographic parameters were evaluated by considering the excitation intensity ratio (*EIR*), I_{274}/I_{268} and is well fit by using the function (Fig. S24b) in equation 15.

$$EIR = A2 + \frac{A1}{1 + e^{\frac{T - A0}{d}}} \tag{15}$$

Where *A0*, *A1*, and *d* are constants while *T* is the temperature. A maximum relative sensitivity of 0.89 %/K was obtained at 240 K, and the results are shown in Fig. S24c.

Spectral shift method

Further, the redshift in the excitation spectra can be ascribed to the relative positions of the transitions from the ground state. At lower temperatures, the excitation transition takes place from the first vibrational level, while at elevated temperatures, the transition takes place from the highly populated higher vibrational levels of the ground state. Consequently, a red shift in the excitation occurs as the increase in temperature favors a shorter energy for the optical absorption. Apart from the *FIR* method, the red shift observed in the excitation spectra around the 268 nm excitation band with respect to the increase in temperature can be used as a tool for probing the temperature so that multi-mode thermometry can be achieved. The excitation maxima shifts from 261 nm to 280 nm as the temperature increases from 80 to 500 K. The maximum peak position with respect to the temperature plot, as shown in Fig. S24d, is fitted with the linear relationship given by $\lambda = 0.05\,T + 254$, where λ is the maximum peak position and *T* is the temperature.

The relative sensitivity S_r is given by the equation 16,[42,43]

$$Sr = \frac{1}{\lambda}\frac{\Delta\lambda}{\Delta T} \times 100\ \% \tag{16}$$
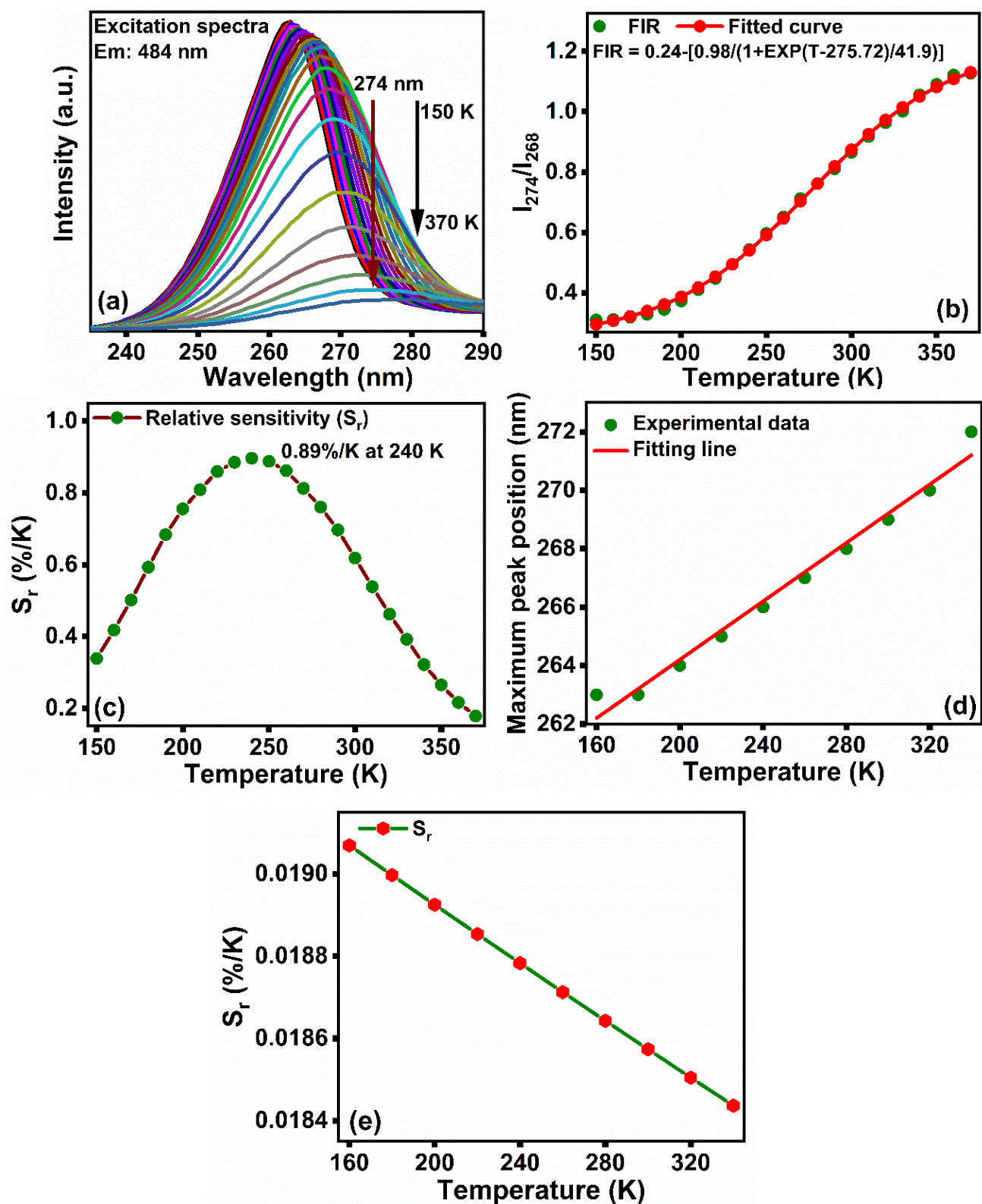
Fig. S24 (a) TDPLE spectra monitored at 484 nm emission wavelength, (b) I_{274}/I_{268} nm vs Temperature plot, (c) S_r based on I_{274}/I_{268} vs Temperature plot, (d) Maximum peak position with respect to temperature, (e) relative sensitivity vs temperature.

The relative sensitivity vs temperature plot is shown in Fig. S24 e and the maximum relative sensitivity of 0.019 %/K was obtained at 160 K. However, the relative sensitivity for the temperature readout using *FIR* and other methods offers more sensitivity than the spectral shift method.

Table S10. List rare earth activated double perovskites reported for optical thermometry.

Phosphor	Temperature Range (K)	Method	Relative sensitivity (*Sr*) (%K^{-1})	References
$BaTiO_3$: Ho^{3+}/Yb^{3+}	298-578	*UCL*	2.78	44
$CaZrO_3$:Bi^{3+}	303-443	*FIR*	1.78	45
$Na0.5Bi_{0.5}TiO_3$:Ho^{3+}/Yb^{3+}	167-377	*FIR*	6.14	46
$(BaSr)TiO_3$: Pr^{3+}	313-413	*FIR*	2.77	47
$CaTiO_3$:Nd^{3+}/Yb^{3+}	323-563 K	*FIR*	1.52	48
$CaTiO_3$: Ni^{2+}	183-473 K	*FIR*	2.44	49
$BaTiO_3$: Ni^{2+}	183 – 473	*FIR*	1.18	49
$CaTiO_3$: Pr^{3+}	298-523	*FIR*	5.2	50
$MgTiO_3$: Ni^{2+}	183-473	*FIR*	1.18	49
La_2MgTiO_6:Pr^{3+}/Dy^{3+}	298-548	*FIR*	2.357	51
Gd_2ZnTiO_6: Pr^{3+}	293-433	*FIR*	1.67	52
$SrLaLiTeO_6$: Mn^{4+}, Dy^{3+}	298-673	*Lifetime*	2.18	53
$BaLaMgNbO_6$:Mn^{4+}/Dy^{3+}	230-470	*Lifetime*	2.43	54
$BaLaMgNbO_6$:Mn^{4+}/Dy^{3+}	230-470	*FIR*	1.82	54
$NaLaMgWO_6$: Er^{3+}/Yb^{3+}	293-573	*FIR*	1.41	55
$CaGdMgSbO_6$:Mn^{4+}/Sm^{2+}	298-573	*FIR*	1.54	56
$LiLaMgWO_6$: Pr^{3+}	293-573	*FIR*	3.25	57
La_2MgTiO_6:V^{5+}/Cr^{3+}	75-350	*FIR*	1.96	58
$NaLaMgWO_6$:Mn^{4+}/Er^{3+}	303-523	*FIR*	1.31	59
$CsPbCl_3$:Mn^{2+}@glass	80-143 K	*FIR*	10.04	60
$CsPbI_3$:Tb^{3+} @ glass	293-453	*FIR*	7.12	61

Table S11. Comparison of the relative sensitivity of various temperature sensors with the BMTO: $0.02Eu^{3+}$.

Phosphor	Temperature Range (K)	Method	Relative sensitivity (*Sr*) (%K^{-1})	References
Sr_2CdTeO_6: Eu^{3+}	*300 - 500*	*FIR*	0.28	[31]
Ba_2MgWO_6: Eu^{3+}	*80-160*	*FIR*	1.5 (120 K)	[62]
$Ba_2Y_{2/3}TeO_6$: Eu^{3+}	*300-500*	*FIR*	0.18 (300 K)	[63]
La_2MgTiO_6: Eu^{3+}	*77-450*	*FIR*	3 (77 K)	[64]
$BaTiO_3$: Eu^{3+}	*10-300*	*RPIR*	2.5 (75 K)	[65]
$GdAlO_3$: Eu^{3+}	*620-793*	*Lifetime*	2.28 (793 K)	[66]
Sr_2GaNbO_6: Eu^{3+}	*298-623*	*FIR*	1.86 (298 K)	[67]
La_2ZnTiO_6: Eu^{3+}/Bi^{3+}	*298-450*	*FIR*	1.5 (293 K)	[68]
$CaLaMgTaO_6$: Eu^{3+}/Bi^{3+}	*393-573*	*FIR*	1.33 (483 K)	[69]
Ca_2MgWO_6: Eu^{3+}/Bi^{3+}	*298-523*	*FIR*	8.52 (323 K)	[70]
$SrGdLiTeO_6$: $Eu^{3+,}Mn^{4+}$	*298-573*	*Lifetime*	0.229(573 K)	[71]
$SrGdLiTeO_6$: $Eu^{3+,}Mn^{4+}$	*300-550*	*FIR*	4.9 (550 K)	[71]
Ba_2LaNbO_6: $Eu^{3+,}Mn^{4+}$	298-498	*FIR*	2.08 (398 K)	[72]
$NaLaMgWO_6$: $Eu^{3+,}Mn^{4+}$	303-523	*FIR*	0.86 (523 K)	[73]
Ba_2YNbO_6: $Eu^{3+,}Mn^{4+}$	303-483	*FIR*	1.86 (463 K)	[74]
La_2LiSbO_6: $Eu^{3+,}Mn^{4+}$	303-523	*FIR*	0.891(523 K)	[75]
$SrLaLiTeO_6$: $Eu^{3+,}Mn^{4+}$	200-360	I_{CTB}/I_{Eu} $^{3+}$	1.97 (200 K)	[36]
Ba_2MgTeO_6: Eu^{3+}	100 – 300	*FIR*	0.34 (140 K)	[This work]
Ba_2MgTeO_6: Eu^{3+}	200 – 350	*FIR*	3.16 (350 K)	[This work]
Ba_2MgTeO_6: Eu^{3+}	150 – 420	*EIR*	4.86 (390 K)	[This work]
Ba_2MgTeO_6: Eu^{3+}	160 - 340	*Spectral shift method*	0.019(160 K)	[This work]

Reference

1. S. Vasala and M. Karppinen, *Prog. Solid State Chem.*, 2015, **43**, 1.

2. A. Dias, G. Subodh, M. T. Sebastian, M. M. Lage and R. L. Moreira, *Chem. Mater.*, 2008, **20**, 4347.

3. J. Liang, S. Zhao, X. Yuan and Z. Li, *Optics & Laser Technology*, 2018, **101**, 451.

4. V.L. Vilesh and G. Subodh, *Ceramics International*, 2018, **44**, 12036.

5. A. Yao, X. Zhou, W. Wu, H. Song, Y. Hong, S. Hu, B. Wang, S. Lu and Y. Wang, *Chemical Physics*, 2021, **546**, 111170.

6. X. Zhou, B. Wang, A. Yao, S. Lu, Y. Hong, S. Hu, J. Cheng, Y. Wang and C. Wang, *Journal of Luminescence*, 2021, **240**, 118458.

7. H. Song, W. Wu, Z. Xing, X. Zhou, A. Yao, S. Hu, Y. Hong, B. Wang, S. Lu and Y. Wang, *Ceramics International*, 2021, **47**, 17286.

8. G. Zhou, Y. Huang, D. Wei, S. Bi and H. J. Seo, *J. Materials and Design*, 2019, **181**, 108066.

9. X. Yun, J. Nie, H. Hu, H. Zhong, D. Xu, Y. Shi and H. Li, *Nanomaterials*, 2024, **14**, 46.

10. S. Gong, R. Wu, Q. Han, D. Kong and W. Wu, *J. Mater. Chem. C*, 2022, **10**, 13217.

11. T. Chang, Q. Wei, R. Zeng, S. Cao, J. Zhao and B. Zou, *J. Phys. Chem. Lett.*, 2021, **12**, 1829.

12. J. S. Nithin, A. Bindhu, K. S. Sibi, K. G. Gopchandran and S. Ganesanpotti, Indian Pat. (2023) 454107. https://drive.google.com/file/d/1LBdYloJA-MTkVT-RK_RcGt0PR5apg8ky/view?usp=sharing.

13. S. C. Lal, I. N. Jawahar, S. Ganesanpotti, Dalton Transactions, 2024, 53 1230–1244.

14. Suraja, N. J., Bindhu, A., Solaman, S. K., & Ganesanpotti, S. *Journal of Luminescence*, 2024, **277**, 120889.

15. Cavalli, E., Mezzadri, F., & Natile, M. (2024). *Optical Materials X*, 2024, **23**, 100337.

16. D. Huang, P. Zhao, Z. Wang, L. Song, Y. Jin, J. Gao, Solid State Sciences, 2024, 107553.

17. K. H. Tam, C. K. Cheung, Y. H. Leung, A. B., Djurisic, C. C. Ling, C. D. Beling, S. Fung, W. M. Kwok, W. K. Chan, D. L. Phillips, L. Ding, W. K. Ge, The Journal of Physical Chemistry B, 2006, **110**, 20865–20871.

18. L. Zhang, Y. Xie, X. Geng, B. Deng, H. Geng and R. Yu, *Journal of Luminescence*, 2020, **225**, 117365.

19. B. Amrithakrishnan and G. Subodh, *Mater. Res. Bull.*, 2017, **93**, 177.

20. P. Dang, G. Li, X. Yun, Q. Zhang, D. Liu, H. Lian, M. Shang and J. Lin, *Light: Science & Applications*, 2021, **10**, 29.

21. S. Wang, Y. Xu, T. Chen, W. Jiang, J. Liu, X. Zhang, W. Jiang, L. Wang, *Chem. Eng. J.*, 2021, **404**, 125912.

22. X. Wang, F. Jahanbazi, J. Wei, C. U. Segre, W. Chen and Y. Mao, *ACS Appl. Mater. Interfaces*, 2022, **14**, 36834.

23. S. C. Lal, V. Lalan and S. Ganesanpotti, *Inorg. Chem.*, 2018, **57**, 6226.

24. H. W. Eng, P. W. Barnes, B. M. Auer and P. M. Woodward, *J. Solid State Chem.*, 2003, **175**, 94.

25. Z.W. Zhang, D.Q. Ma, Y. Yue, M.Z. Ma and R.P. Liu, *Journal of Alloys and Compounds*, 2015, **636**, 113-116.

26. Yang, C., Fan, C., Hussain, F., Sheng, W., Song, K., Wu, J., Huang, Q., Su, W., Xu, J., Sun, S., & Wang, D. *Journal of Rare Earths*, 2022, **41**, 489–497.

27. Ishigaki, T., Matsushita, N., Yoshimura, M., Uematsu, K., Toda, K., & Sato, M. *Physics Procedia*, 2009, **2**, 587–601.

28. J. Liang, S. Zhao, X. Yuan and Z. Li, *Optics & Laser Technology*, 2018, **101**, 451-456.

29. L. Zhang, Y. Xie, X. Geng, B. Deng, H. Geng and R. Yu, *Journal of Luminescence*, 2020, **225**, 117365.

30. Y. Wei, Z. Liu, C. Sun, X. Ding, S. Wu, R. Chen, F. Wang, H. Wang, X. Xing and L Huang, *Adv. Funct. Mate,*. 2024, 2401664.

31. N. J. Suraja, A. Mahesh, K. S. Sibi and S. Ganesanpotti, *Journal of Alloys and Compounds*, 2021, **865**, 158902.

32. C. Yue, D. Zhu, Q. Yan and Y. Pu, *RSC Adv.*, 2019, **9**, 26364.

33. R. G. A. Kumar, S. Hata, K. Ikeda and K. G. Gopchandran, *Ceram. Int.*, 2015, **41**, 6037.

34. M. D. Dramicanin, L. Marciniak, S. Kuzman, W. Piotrowski, Z. Ristic, J. Perisa, I. Evans, J. Mitric, V. Đorđevic, N. Romcevic, M. G. Brik and C. G. Ma, *Light: Science & Applications*, 2022, **11**, 279.

35. S. Goderski, M. Runowski, P. Wozny, V. Lavin and S. Lis, *ACS Appl. Mater. Interfaces*, 2020, **12**, 40475.

36. S. C Lal, J. I. Naseemabeevi and S. Ganesanpotti, *Journal of Science: Advanced Materials and Devices*, 2023, **8**, 100544.

37. A. Kabanski, M. Ptak and D. Stefanska, *ACS Appl. Mater. Interfaces*, 2023, **15**, 7074.

38. Y. Gao, F. Huang, H. Lin, J. Zhou, J. Xu and Y. Wang, *Adv. Funct. Mater.*, 2016, **26**, 3139.

39. Z. Antic, M. D. Dramicanin, K. Prashanthi, D. Jovanovic, S. Kuzman and T. Thundat, *Adv. Mater.*, 2016, **28**, 7745.

40. D. Duan, Y. Wang, S. Jiang, L. Li, G. Xiang, X. Tang, Y. Li and X. Zhou, *J. Lumin.*, 2019, **215**, 116636.

41. S. Zhou, C. Duan and S. Han, *Dalton Trans.*, 2018, **47**, 1599.

42. P. Yang, L. Li, Y. Deng, Y. Wang, S. Jiang, X. Luo, G. Xiang, Y. Lu and X. Zhou, *Dalton Trans.*, 2019, **48**, 10824.

43. A. Bindhu, J. I. Naseemabeevi and S. Ganesanpotti, *Adv. Photonics Res.*, 2022, **3**, 2100159.

44. T. Zheng, M. Runowski, I.R. Martín, S. Lis, M. Vega, and J. Llanos, Advanced Optical Materials, 2021, **9**, 2100386.

45. X. Tian, H. Dou, and L. Wu, Journal of Materials Science: Materials in Electronics, 2020, **31**, 3944-3950.

46. Y. Wang, C. Ma, Z. Feng, C. Zuo, Ye, Wanggui, C. zhao and Y. Cao, *Journal of Materials Chemistry C*, 2021, **9**, 1353-1361.

47. W. Tang, C. Zuo, Y. Li, C. Ma, X. Yuan, Z. Wen and Y. Cao. *Journal of Luminescence*, 2021, **236**, 118103.

48. Y. Luo, Y. Liu, C. Wang, G. Bai, Y. Shen, Z. Jiang and L. Chen, *Sensors and Actuators A: Physical*, 2021, **326**, 112741.

49. C. Matuszewska and L. Marciniak, *Journal of Luminescence*, 2020, **223**, 117221.

50. X. Tian, S. Lian, C. Ji, Z. Huang, J, Wen, Z. Chen, H. Peng, S. Wang, J. Li, J. Hu and Y. Peng, *Journal of Alloys and Compounds*, 2019, **784**, 628-640.

51. H. Zhang, Y. Liang, H. Yang, S. Liu, H. Li, Y. Gong and G. Li, *Inorganic chemistry*, 2020, **59**, 14337-14346.

52. Y. Gao, Y. Cheng, T. Hu, Z. Ji, H. Lin, J. Xu and Y. Wang, *Journal of Materials Chemistry C*, 2018, **6**, 11178-11183.

53. Z. Wu, L. Li, G. Tian, Y. Wang, F. Ling, Z. Cao and X. Zhou, *Dalton Transactions*, 2021, **50**, 11412-11421.

54. Y. Lin, L. Zhao, B. Jiang, J. Mao, F. Chi, P. Wang and M. Yin, *Optical Materials*, 2019, **95**, 109199.

55. W. Ran, H.M. Noh, S.H. Park, B.C. Choi, J.H. Kim, J.H. Jeong and J. Shi, *Dalton Transactions*, 2019, **48**, 11382-11390.

56. J. Liao, M. Wang, L. Kong, J. Chen, X. Wang, H. Yan and C. Tu, *Journal of Luminescence*, 2020, **226**, 117492.

57. J. Wang, N. Chen, J. Li, Q. Feng, R. Lei, H. Wang and S. Xu, S. *Journal of Luminescence*, 2021, **238**, 118240.

58. D. Stefańska, B. Bondzior, T.H.Q. Vu, M. Grodzicki and P.J. Deren, *Dalton Transactions*, 2021, **50**, 9851-9857.

59. Y. Zhang, N. Guo, B. Shao, J. Li, R. Ouyang and Y. Miao, *Spectrochimica Acta Part A: Molecular and Biomolecular Spectroscopy*, 2021, **259**, 119797.

60. B. Zhuang, Y. Liu, S. Yuan, H. Huang, J. Chen, J and D. Chen, D, *Nanoscale*, 2019, **11**, 15010-15016.

61. Q. Yang, L. Zhao, Z. Fang, Z. Yang, J. Cao, Y. Cai, X. Xu, *Journal of Rare Earths*, 2021, **39**, 712-717.

62. D. Stefanska, B. Bondzior, T.H.Q. Vu, N. M. Gawel and P.J. Deren, *Journal of Alloys and Compounds*, 2020, **842**, 155742.

63. S. C. Lal, J. I. Naseemabeevi and S. Ganesanpotti, *Materials Advances*, 2021, **2**, 1328.

64. B. Bondzior, D. Stefanska, T.H.Q. Vũ, N. M. Gaweł, P.J. Deren, *Journal of Alloys and Compounds*, 2021, **852**, 157074.

65. D. Arnab and R. Ranjan, *Materials Horizons*, 2020, **7**, 1101.

66. V. Lojpur, S. Culubrk, M. Medic and M. Dramicanin, *Journal of Luminescence*, 2016, **170**, 467.

67. Q. Chen, X. Yang, G. Zhang, Q. Ma, S. Han and B. Ma, *Optical Materials*, 2021, **111**, 110585.

68. J. Wang, R. Lei, S. Zhao, F. Huang, D. Deng, S. Xu and H. Wang, *Journal of Alloys and Compounds*, 2021, **881**, 160601.

69. C. Xu, C. Li, D. Deng, H. Yu, L. Wang, C. Shen, X. Jing and S. Xu, *Journal of Luminescence*, 2021, **236**, 118096.

70. M. Cui, J. Wang, J. Li, S. Huang and M. Shang, *Journal of Luminescence*, 2019, **214**, 116588.

71. L. Li, G. Tian, Y. Deng, Y. Wang, Z. Cao, F. Ling, Y. Li, S. Jiang, G. Xiang and X. Zhou, *Opt Express*, 2020, **28**, 33747.

72. P. Wang, J. Mao, L. Zhao, B. Jiang, C. Xie, Y. Lin, F. Chi, M. Yin, and Y. Chen. *Dalton Trans*., 2019, **48**, 10062.

73. H. Zhou, N. Guo, M. Zhu, J. Li, Y. Miao and B. Shao, *J. Lumin*., 2020, **224**, 117311.

74. Y. Hua, T. Wang, W. Xia, J. S. Yu and L. Li, *Mater. Today Chem*., 2022, **23**, 100710.

75. Y. Song, N. Guo, J. Li, R. Ouyang, Y. Miao and B. Shao, *Ceram. Int*., 2020, **46**, 22164.